An implantable ventilator augments inspiration in an *in vivo* porcine model

Lucy Hu[1,2], Jean Bonnemain[2,3], Mossab Y. Saeed[4], Manisha Singh[2], Diego Quevedo Moreno[5], & Ellen T. Roche[2,5]

1. Harvard-MIT Program in Health Sciences & Technology, Massachusetts Institute of Technology, Cambridge, MA 02139.
2. Institute for Medical Engineering & Science, Massachusetts Institute of Technology, Cambridge, MA 02139.
3. Department of Adult Intensive Care Medicine, Lausanne University Hospital and University of Lausanne, Lausanne, Switzerland.
4. Department of Cardiac Surgery, Boston Children's Hospital, Harvard Medical School, Boston, MA 02115, USA.
5. Department of Mechanical Engineering, Massachusetts Institute of Technology, Cambridge, MA 02139.

Abstract

Severe diaphragm dysfunction can lead to respiratory failure, requiring permanent mechanical ventilation. Permanent tethering to a mechanical ventilator via a patient's mouth or tracheostomy can interfere with quality of life and autonomy by hindering activities like speech, swallowing, and mobility. We present a diaphragm assist system that intervenes internally at the diaphragm as opposed to the upper airway. By implanting contractile, soft robotic actuators above the diaphragm to push downwards and augment diaphragm motion during inspiration, this diaphragm assist system functions as an implantable ventilator. We demonstrate the proof-of-concept feasibility of this system to augment physiological metrics of ventilation in an *in vivo* porcine model of varied respiratory insufficiency. Synchronized actuation of the assist system with native respiratory effort augmented the tidal volume and was capable of improving minute ventilation into a normal range. A diaphragm assist system has the potential to provide a new therapeutic ventilation option that aims to restore respiratory performance without sacrificing quality of life.

Introduction

The diaphragm is the major muscle responsible for inspiration, and contributes to up to 70% of the inspiratory tidal volume in a healthy individual.[1,2] Diaphragm dysfunction can result from a variety of etiologies including phrenic nerve trauma[3] and neuromuscular disease[4,5]. Owing to the degenerative nature of many of these etiologies, mechanical respiratory failure exists as a continuous spectrum of dysfunction. Severe diaphragm dysfunction or paralysis can lead to chronic respiratory failure. When disease progresses beyond the treatment capacity of noninvasive treatment, patients must make the difficult decision to opt for permanent invasive ventilation via a tracheostomy or to pursue palliative care with an understanding of the terminal nature of their disease. Invasive ventilation can interfere with many aspects of a patient's quality of life, such as hindering speech, requiring full-time care, and possibly necessitating the patient move into a care facility. There is an urgent need for new therapeutic ventilation options that restore respiratory performance without sacrificing quality of life, especially for those with the most severe cases of diaphragm dysfunction.

Respiration is a fundamentally mechanical process. The diaphragm is a dome-shaped muscle that drives up to 70% of respiration[1,6]. Soft robotic actuators are ideal for reproducing complex, repetitive muscle contractions, such as that of the diaphragm, while interfacing nondestructively with biological tissue. Previously, fully implanted soft actuators have shown the ability to augment heart function[7–11] and many other newly developed implantable robotics have shown utility in a broad spread of biological applications[12–20]. Due to the mechanical nature of respiratory failure, especially in the context of conditions like muscular dystrophy, implanted soft robotic actuators applied to the diaphragm have the potential to mechanically support and augment its function. There is minimal prior work investigating soft robotics applied to the augmentation of respiration; one of the few examples reports a dielectric elastomer sheet used to completely replace an excised diaphragm and generate motion. [12,21] Contrastingly, the work presented here leaves the native diaphragm intact while demonstrating function in terms of augmentation of clinically-relevant physiological metrics (ventilation flows, volumes, and pressures) in addition to diaphragm motion in an *in vivo* porcine model as opposed to solely replicating diaphragm motion while excising the native diaphragm.

Here, we demonstrate a diaphragm assist system that functions as an implantable ventilator by using soft robotic actuators to mechanically augment diaphragm function during inhalation, increasing inspiration. As a proof-of-concept, we simulate a range of respiratory insufficiency within each animal—specifically, we induce respiratory depression via anesthetics and diaphragm paralysis by severing the phrenic nerve—and then demonstrate the ability of the assist system to augment respiratory flows, volumes, and pressures. We also investigate specific metrics of inspiratory function including peak inspiratory flow and transdiaphragmatic pressure[22]. We show that in order to achieve effective inspiration assistance, the actuation of the assist system must be synchronized to the subject's underlying respiratory effort. To achieve this, we have built a control system in which actuation is triggered by the beginning of inspiration. Through an analysis of the respiratory waveforms, we investigate the optimal alignment of actuation with the subject's native respiratory effort. By augmenting diaphragm function in a biomimetic fashion, we demonstrate the replication and augmentation of the native biomechanics of respiration in which a negative pleural and alveolar pressure drives airflow, as opposed to the positive pressure ventilation of standard mechanical ventilation.

Results

Soft robotic design strategy applied to mechanically assisting inspiration.

As depicted in the schematic in Fig. 1a, when the diaphragm contracts, the arclength of the diaphragm shortens, and the entire sheet of the diaphragm moves downwards, acting as a pump. The thoracic cavity volume increases and pressure decreases, ultimately driving respiration.

Our strategy aims to harness the contractile function of pneumatic artificial muscles (PAMs) to mimic and augment the native contraction of the diaphragm. We opt for a McKibben type PAM—a classical soft actuator type with a simple fabrication process and high force generation[23,24] that is capable of mimicking and augmenting biological systems.[7,8,13] At their simplest, McKibben actuators are composed of an expandable weaved mesh surrounding a bladder connected to an airline (Fig. 1b) (see Methods). When the bladder is pressurized, the mesh expands radially and drives linear contraction (Fig. 1c). The McKibben actuators used in this work were capable of generating up to 40 N of contractile force under 20 psi pressurization (see Extended Data Fig. 1, and Extended Data Fig. 2, and Supplementary Notes). Conceptually, we harness the linear contraction of these PAMs by placing them superior to the native diaphragm so that the relaxed PAM conforms to the native curvature of the diaphragm (Fig. 1d). Mimicking the native diaphragm, we anchor the ends of the PAMs to the ribs (see Methods). With pressurization, the length of the PAM shortens, the arclength shortens, and the PAM mechanically pushes the diaphragm downwards (shown *in situ* in Fig. S1). Actuator behavior is governed by the degree of pressurization. Set pressurization waveforms are programmed to the control system and electropneumatic regulators. *In vitro* and *in vivo* characterization of actuator behavior when controlled by different pressurization waveforms is included in the Extended Data (Extended Data Fig. 1 and Extended Data Fig. 2).

In contrast to the dielectric artificial diaphragm described by Bashkin, et al.,[12] our diaphragm assist system uses a set of two linear PAMs, leaves the native diaphragm intact, and has a low profile presence (deflated: 5 mL volume, inflated: 17 mL volume). To test this concept in a live porcine model, we surgically implanted a pair of McKibben actuators in an anterior-to-posterior direction lateral to the heart. The actuator placement is visualized in a 3D rendering in Fig. 1e. Fluoroscopy of the diaphragm was taken throughout the experiments. The lateral cross-sectional view from the fluoroscopy shows the realization of our soft robotic strategy in an *in vivo* pig model (Fig. 1f,g).

The actuators push the diaphragm caudally, augmenting the diaphragm displacement. Ultrasonography is used to visualize and quantify diaphragm displacement (Fig. 2). The coronal plane cross section of the actuator and the diaphragm is visualized via two-dimensional (B-mode, brightness) ultrasonography of the diaphragm (Fig. 2a,b). To quantify the motion of the device and the diaphragm, we used the (M-mode, motion) ultrasonography (Fig. 2c,d), which visualizes the image along a single line – selected within the B-mode image – over time. M-mode features excellent axial and temporal resolutions, and is particularly well-suited for motion analysis[25]. The actuator augments the diaphragm displacement per breath from 0.37 cm displacement of unassisted ventilation (Fig. 2c) to 1.92cm displacement of assisted ventilation (Fig. 2d).

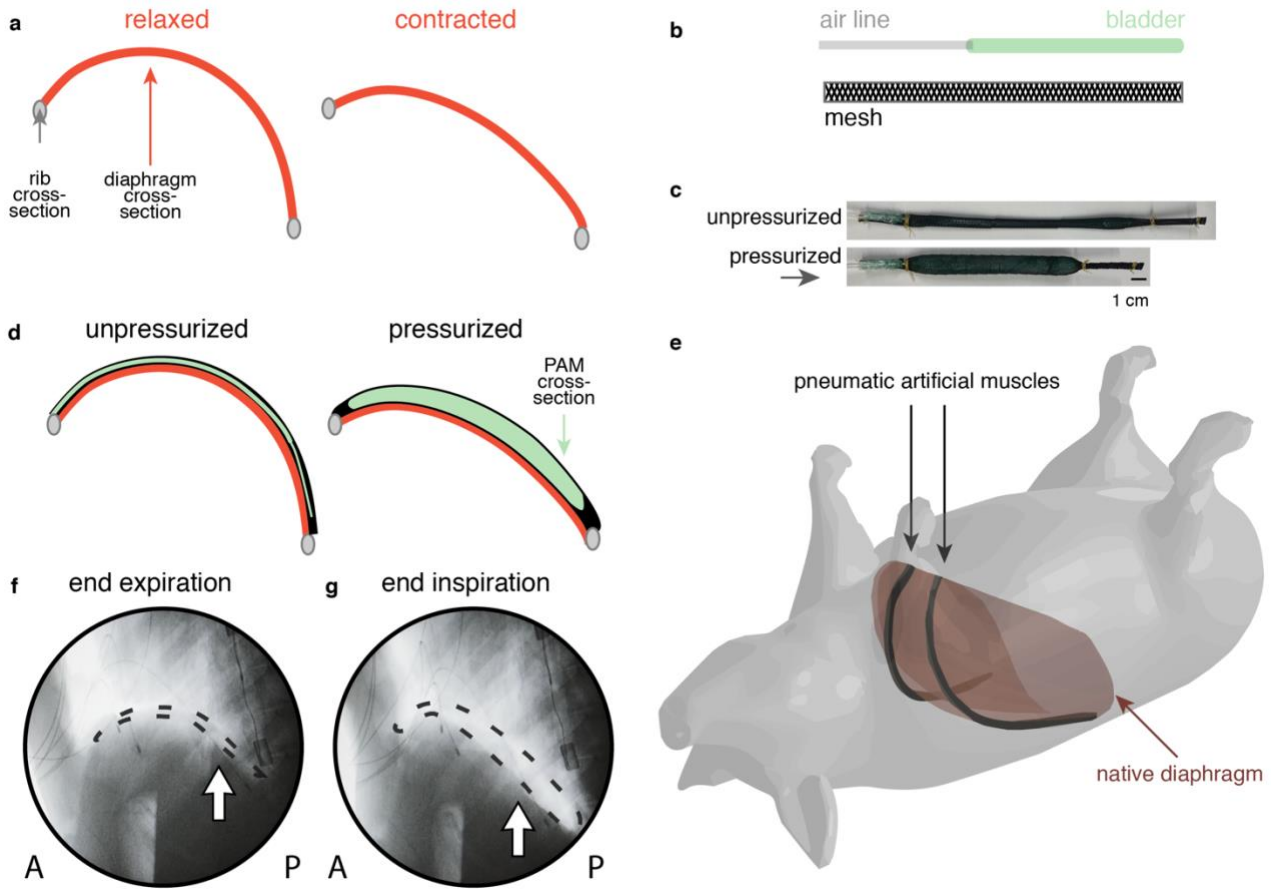

Fig. 1: Overview of using implantable pneumatic artificial muscles for augmenting respiratory muscle function. a, Schematic depicting the lateral cross-sectional of the native diaphragm anchored to the ribs in a relaxed (left) and contracted (right) state. **b** Schematic of the components that makeup a single pneumatic artificial muscle (PAM). **c,** Pictures of a single PAM in an unpressurized and pressurized state. **d,** Lateral cross-sectional schematic of the strategy to augment diaphragm motion by placing PAMs superior to the diaphragm. The PAM conforms to the relaxed diaphragm in its unpressurized (left) state and pushes the diaphragm caudally in its pressurized (right) state. **e,** Visualization of the placement of PAMs (in black) superior to the diaphragm in a live pig model. **f, g,** Lateral fluoroscopy view of the *in vivo* porcine diaphragm with PAMs in an (**f**) unpressurized and (**g**) pressurized state (fluoroscopic videos available as Supplementary Video 1). The air-filled balloon of the actuator is outlined with a dashed line and indicated with an arrow. *A* and *P* indicate the anterior and posterior direction of the animal.

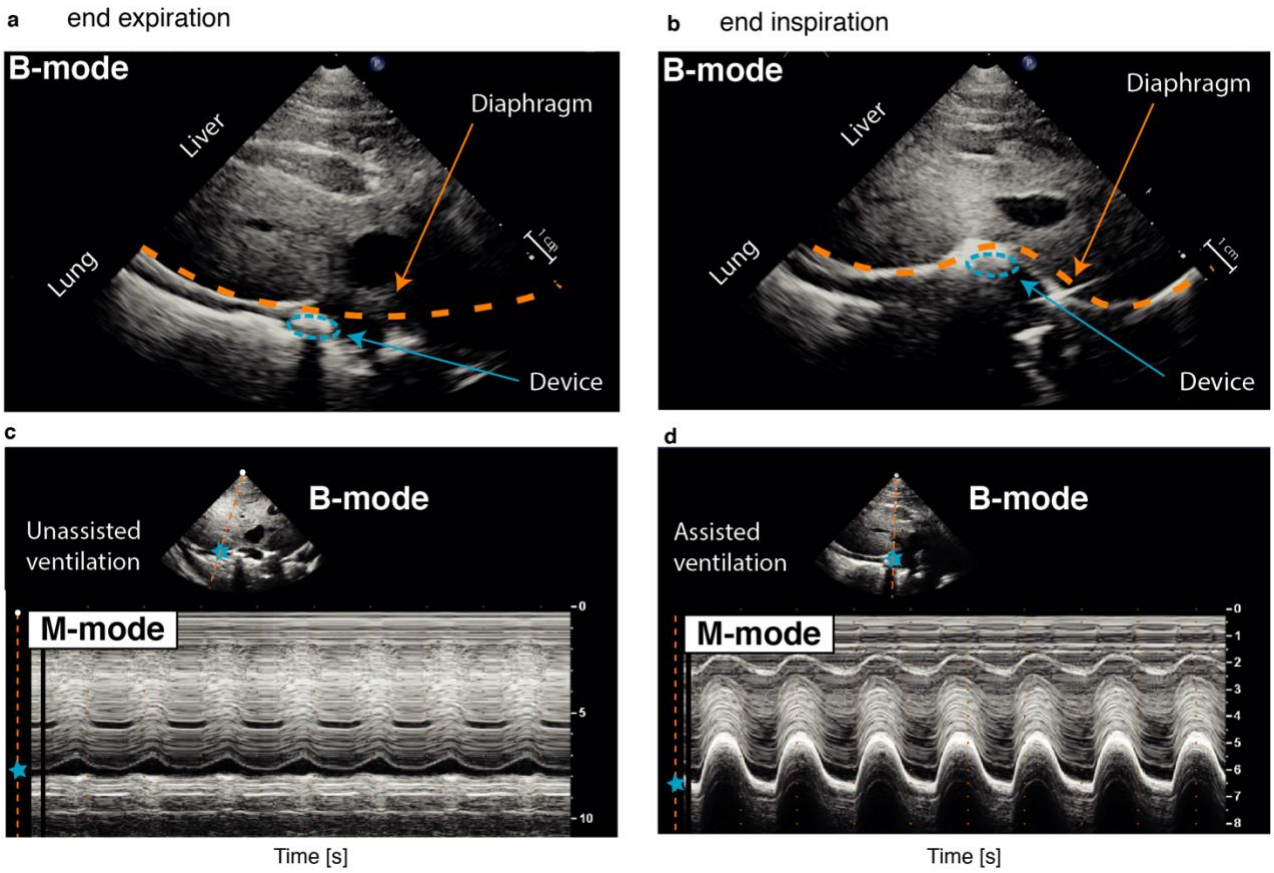

Fig. 2: Ultrasound imaging of the diaphragm and its associated displacement with and without assisted ventilation. (a-b): Two-dimensional view (B-mode) of the diaphragm at **(a)** the end of expiration (device not pressurized, muscle relaxed) and **(b)** at the end of inspiration (device pressurized, muscle contracted). **(c-d)** M-mode evaluation of diaphragm motion during **(c)** unassisted ventilation, and **(d)** assisted ventilation (20 psi). For all images, the probe was positioned in the right subcostal space, pointing toward the cranial direction. Orange dashed line: diaphragm, blue dashed ellipse: actuator cross-section, blue star: spatial position of the diaphragm.

Augmenting tidal volume and peak inspiratory flow in vivo.
To evaluate the ability of our diaphragm assist system to augment respiratory function, the animals were instrumented to collect physiological data, including respiratory flows, volumes, and pressures within the respiratory system (Fig. S2). The pressurization of the soft robotic actuators was controlled via a custom-built control system; the actuation pressure data was input into the same high-resolution data acquisition system as the physiological data (see Methods).

Ventilation is key to driving CO_2 exchange, so we first examine the flow and volume waveforms as metrics of ventilatory function. Flow is measured by a spirometer. Peak inspiratory flow can be used as a clinical metric of inspiratory function[22], which yields a direct measurement of the effect of the diaphragm assist system. Integrating the flow with respect to time yields a volume waveform over time. The volume of each breath (tidal volume) and its rate (minute ventilation) are the most relevant parameters of directly measuring ventilation. Pressures within the respiratory system, such as pleural and abdominal pressures, reveal information about the respiratory biomechanics that physically drive ventilation and are discussed later in this work.

To start each study, the animal was anesthetized appropriately with isoflurane and placed on mechanical ventilation. Isoflurane induces a respiratory depression with decreased tidal volumes and increased respiratory rate that ultimately combine to a reduced minute ventilation[26]. The respiratory depression secondary to the isoflurane is used as our baseline animal model of respiratory insufficiency due to hypoventilation. Each subject has a reduced but non-zero respiratory drive and response to CO_2. Mechanical ventilation is used to support the animal throughout the implantation surgery. Within each subject, we introduce a series of respiratory challenges, collecting data during periods of unassisted ventilation (in which any spontaneous respiration is due to the native respiratory drive) and during periods of actuator assisted ventilation. Mechanical ventilation is used to restore and maintain a state of normoventilation after and between respiratory challenges. To investigate the effect of the diaphragm assist system, a representative respiratory challenge was chosen per subject. The phrenic nerve is intact for all data shown in Fig. 3.

In a vignette from the best responding subject (Fig. 3a), we show that the assist system has the direct capacity to augment the peak inspiratory flow from 0.18 L/s to 0.59 L/s and the tidal volume from 55 mL to 161 mL. When the assist is resumed after a short period of unassisted respiration, the augmentation effect of the actuation on the flow and volume waveforms is reestablished nearly immediately over the course of 2 breaths.

An example of a full respiratory challenge is shown in Fig. 3b. During the unassisted ventilation at the start of the challenge, the subject models a state of hypoventilation. During this period, the tidal volumes and flows have a slight increase over time, indicating the baseline respiratory drive is responding to the increasing CO_2 status due to the unassisted low minute ventilation (0.9 L/min). When assist is switched on (as indicated by the actuator pressure waveform, the white background, and the black arrow), there is a clear jump in the peak inspiratory flow (+0.20 L/s, 95%CI +0.19 L/s to +0.22 L/s), tidal volumes (63mL, 95% CI 58 mL to 68 mL), and minute ventilation (0.9 L/min to 3.1 L/min). The actuators cycle between a pressurized and unpressurized state for 10 minutes. At the end of the respiratory challenge when the respiratory effort has reached a steady state, the assist is switched off and we see that the respiratory effort drops slightly (peak inspiratory flow: -0.09 L/s, 95%

CI -0.08 to -0.10; tidal volume: -10 mL, 95% CI -7 to -13) but much less than the jump seen at the start of the respiratory challenge.

The respiratory drive is a slow but dynamic factor underlying all of the respiratory physiology data. As seen in the first 200 s of Fig. 3b, the respiratory drive visibly increases as the low minute ventilation leads to CO_2 buildup. This response to CO_2 is dynamic and varies between subjects based on each animal's response to isoflurane. By examining the breaths immediately before and after these transition points (off-to-on and on-to-off), we can examine the direct effect of the diaphragm assist system in terms of augmenting volume and peak inspiratory flow while minimizing the influence of the changing baseline.

This analysis was conducted for one representative respiratory challenge per each of 5 subjects. These 5 subjects represent the subset of experiments conducted with uninterrupted respiratory challenges that collected the unassisted baseline data both before and after device assistance. We see a spectrum of responsiveness to the diaphragm assist system across subjects (Fig. 3c,d,e). The subjects are ordered from largest change in tidal volume at the start of the challenge to the smallest (best responder to worst responder according to Fig. 3d). We find the diaphragm assist system generates much larger respiratory augmentations at the beginning of a trial—when mechanical ventilation support has just been removed, minute ventilation drops suddenly, and the animal's CO_2 state rises rapidly—than at the end of the respiratory challenge when the respiratory baseline is relatively more stabilized (Fig. 3c,d,e).

Subject A was much more responsive to the assist system than any other subject. In terms of tidal volume, 4 of the 5 subjects show an augmentation of >30 mL per breath at the beginning, whereas only 1 of the subjects shows substantial augmentation to the tidal volume at the end. Of the 4 less responsive subjects (B,C,D,E), 3 of them show a mild response at the end while in the worst responder (E), the actuation overall decreased the ventilation metrics (Fig. 3c-e). The subject with the weakest response had the highest baseline weight-normalized minute ventilation at the beginning of the trial (Fig. 3e) compared to other subjects.

Body weight normalized minute ventilation is used to compare these results to normal physiology. Minute ventilation is a metric of the ventilation rate, taking into account both tidal volume and the respiratory rate. In a normal, conscious pig, the expected body weight normalized minute ventilation is 198 mL/min/kg $\pm$ 41 mL/min/kg with a range of 104 mL/min/kg to 262 mL/min/kg[27], indicated by the green shading in Fig. 3e. Actuator assisted ventilation allowed all 5 subjects to reach the lower range of normal physiology, and 2 of the subjects even achieved a minute ventilation corresponding to one standard deviation below the normal mean (Fig. 3e). However, we note that this minute ventilation is achieved with low tidal volumes and high respiratory rates, which results in a lower alveolar ventilation than the same minute ventilation achieved with high tidal volumes and low respiratory rates.

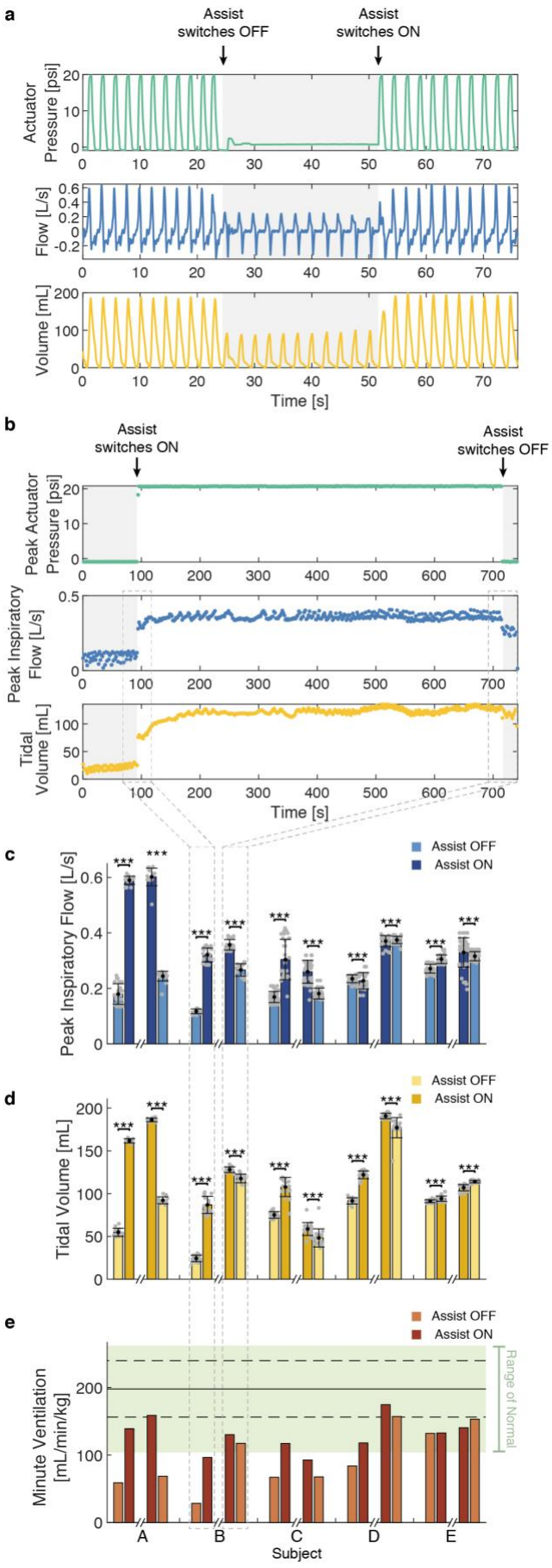

Fig. 3: Ability to augment tidal volume and peak inspiratory flow *in vivo*. a, A representative, continuous segment of actuation pressure, flow, and tidal volume waveforms from the respiratory challenge with the largest augmentation. Gray shading indicates the period of time where the diaphragm assist system is off, and the subject's respiration is unsupported. **b,** A representative set of peak actuation pressure, peak inspiratory flow, and tidal volumes for one full respiratory challenge. Gray shading indicates the period of time where the system is off, and respiration is unassisted. **c,d,** Comparison of the average (**c**) peak inspiratory flow and (**d**) tidal volume in the 30 second period immediately before and after the point where the assist is turned on at the beginning (left two bars per subject) and off at end (right two bars per subject) of the respiratory challenge (as represented by the arrows in **b** and the gray dashed lines in b-e) across 5 subjects (*n* = 11-27 breaths). Each gray dot represents one breath. **e,** Body weight normalized minute ventilation achieved during the 30 second period immediately before and after the assist is turned on at the beginning and off at the end of the respiratory challenge. The range of normal minute ventilation, as reported by Hannon et al[27], is indicated by the light green shading; the solid line indicates the mean; the dashed lines indicate the standard deviation. In **c**-**d,** bar plots show mean ± s.d., ***p<0.001 using a Wilcoxon rank-sum test.

Synchronizing with the underlying respiratory effort.
Like with standard mechanical ventilation[28,29], patient-ventilator synchrony in our system is critical to the ability to augment respiration. Asynchronous ventilation can destructively interfere with the underlying respiratory effort, leading to worse ventilation with assistance than without.

In order to synchronize the actuation of our assist system with the subject's underlying respiratory effort, we built a control system (Fig 4a,b) that can actuate based on the respiratory flow rate. The system uses the spirometry flow sensor as the source data. The flow data is read into our data acquisition system. The associated data analysis software allows a user-set threshold voltage; this threshold voltage was manually titrated during every respiratory trial to achieve qualitatively good synchronization. When the flow rate passes this set threshold, a digital pulse is triggered and sent to the microcontroller in our control box. The microcontroller triggers a pre-set actuation pressure waveform of one cycle of pressurization and depressurization in the electropneumatic regulator, filling and emptying the PAMs with pressurized air (further details in Methods).

Our control system can implement both a set, rhythmic control scheme independent of the native respiratory effort or a dynamic control scheme synchronized with the underlying respiratory effort. Due to the phase and frequency mismatch between the independent actuation and the underlying respiratory effort, the mixed interference of the actuator and the underlying respiratory effort can be seen in both the flow and volume waveform (Fig. 4c). Contrastingly, the well synchronized actuation reveals much more homogenous flow and volume waveforms. (Fig. 4d).

Within each subject, we compare the tidal volumes and peak inspiratory flows in one representative challenge of independent actuation with one representative challenge of synchronized actuation (details in methods). We find that synchronized actuation consistently produces much less variance in the tidal volumes (Fig 4e,f). Although in some subjects—such as subject A—independent actuation achieved a few higher maximum tidal volumes, the independent actuation also achieved lower minimum tidal volumes across all subjects due to the misalignment of actuations with the underlying respiratory effort leading to destructive interference or due to actuation with no underlying breath—representing a breath that is solely actuator driven. Misalignment between the diaphragmatic contraction and the device during independent actuation can be observed with M-mode ultrasound (Fig 4g), in contrast to synchronized actuation (Fig 4h). Asynchronous moments of native diaphragm contraction produce to a heterogenous waveform, and indicated by the orange arrows in Fig. 4g.

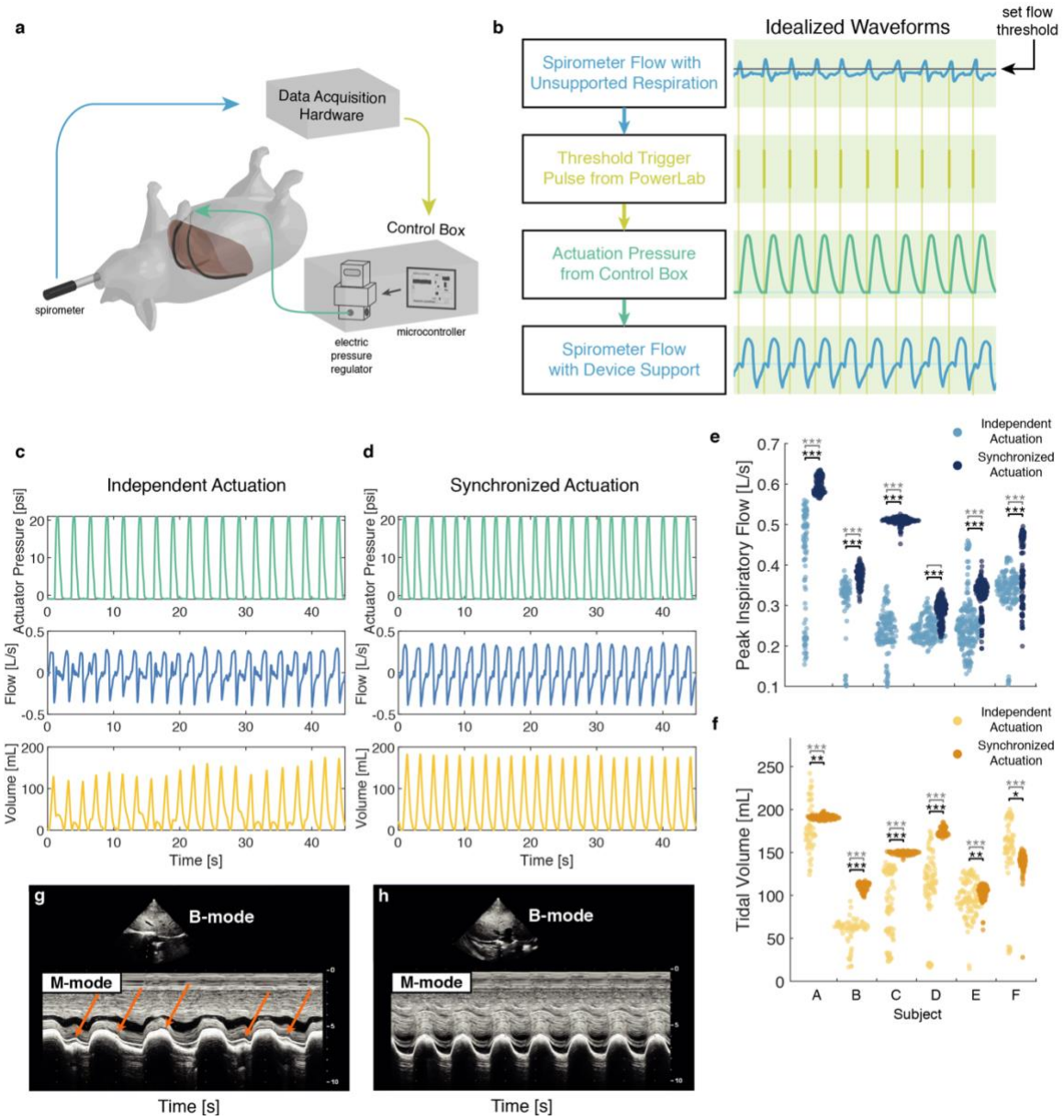

Fig. 4: Synchronous actuation with the native respiratory effort. a, Schematic of the control system. The spirometry flow sensor data is fed into the data acquisition system; when the flow sensor crosses a set threshold a trigger pulse is sent to the control box which triggers a set pressure actuation curve in the electropneumatic regulator, modulating the pressure inside the pneumatic artificial muscles. **b**, A set of idealized waveforms (indicated by the green background) showing the mechanism of synchronization. **c**,**d**, A representative set of collected waveform data—actuation pressure, flow, and tidal volume—for (**c**) a set independent actuation scheme and (**d**) a synchronized actuation scheme. **e,f,** A swarm plot comparing the steady state (**e**) tidal volumes and (**f**) peak inspiratory flows generated with independent actuation and with synchronized actuation for 6 different subjects (*n* = 119 - 419 breaths). **g,h** M-mode analysis during independent (**g**) or synchronized (**h**) actuation. Orange arrows point toward asynchronous diaphragmatic muscle contraction. In e and f, steady state data is taken from 5 minutes to the end of the respiratory challenge. Each dot is one breath. Black significance bars are results from Welch's t-test comparing means. Gray significance bars are results from a 2-sample F-test for equal variances comparing variances. Significance is indicated by *p<0.05,**p<0.01,***p<0.001 for both statistical tests.

Effect of synchronization on blood gas exchange

Physiologically, ventilation is necessary to bring in oxygen (O_2) and to clear out accumulated carbon dioxide (CO_2) from the blood. Arterial blood gases (ABGs) are discrete blood analyses that give a snapshot view of the gas exchange and acid-base homeostasis, providing measurement of partial pressure of O_2 (P_aO_2) and CO2 (P_aCO_2), pH, and bicarbonates (HCO_3^-) in arterial blood. P_aCO_2 is directly and inversely proportional to alveolar ventilation and is therefore a representative metric of ventilatory function. Only pH and pCO_2 are depicted here in Fig. 5, but the full ABG parameters are reported in Extended Data Table 1 and discussed in the Supplementary Notes.

As shown in the prior section, the high variance from independently actuated ventilation showed mixed constructive and destructive interference (Fig. 4e,f) which led to worse ventilation outcomes. The same variance in the peak inspiratory flows and tidal volumes over time due to independent vs. synchronized actuation can be seen in Fig. 5a and Fig. 5b. In these two respiratory challenges, the subject was switched directly from the standard mechanical ventilation to our diaphragm assist system, evaluating its ability to maintain gas exchange.

In the respiratory challenge operated with independent actuation (Fig. 5a), we see high levels of hypercarbia over time. As a result, respiratory acidosis develops, which is a direct consequence of increased P_aCO_2 (Extended Data Table 1a). Contrastingly, in a respiratory challenge operated with synchronized actuation in the same animal (Fig. 5b), pCO_2 levels are relatively well maintained. The acidemia observed for this trial is rather of metabolic cause (called metabolic acidosis) (Extended Data Table 1b, see Supplementary Notes).

In another experiment, a respiratory trial was initiated with 2 minutes of unsupported ventilation and then switched to our diaphragm assist system, evaluating its ability to recover from a period of unsupported ventilation. During the 2 minutes of unsupported ventilation, high levels of CO_2 accumulate quickly over this brief amount of time (Fig. 5c). After two minutes, the diaphragm assist system is actuated with synchronized actuation. The increasing acidification and accumulation of CO_2 reverses and some recovery from the hypercarbic state is seen in the first 10 minutes, with a slight uptick in the CO_2 around 15 minutes into the challenge.

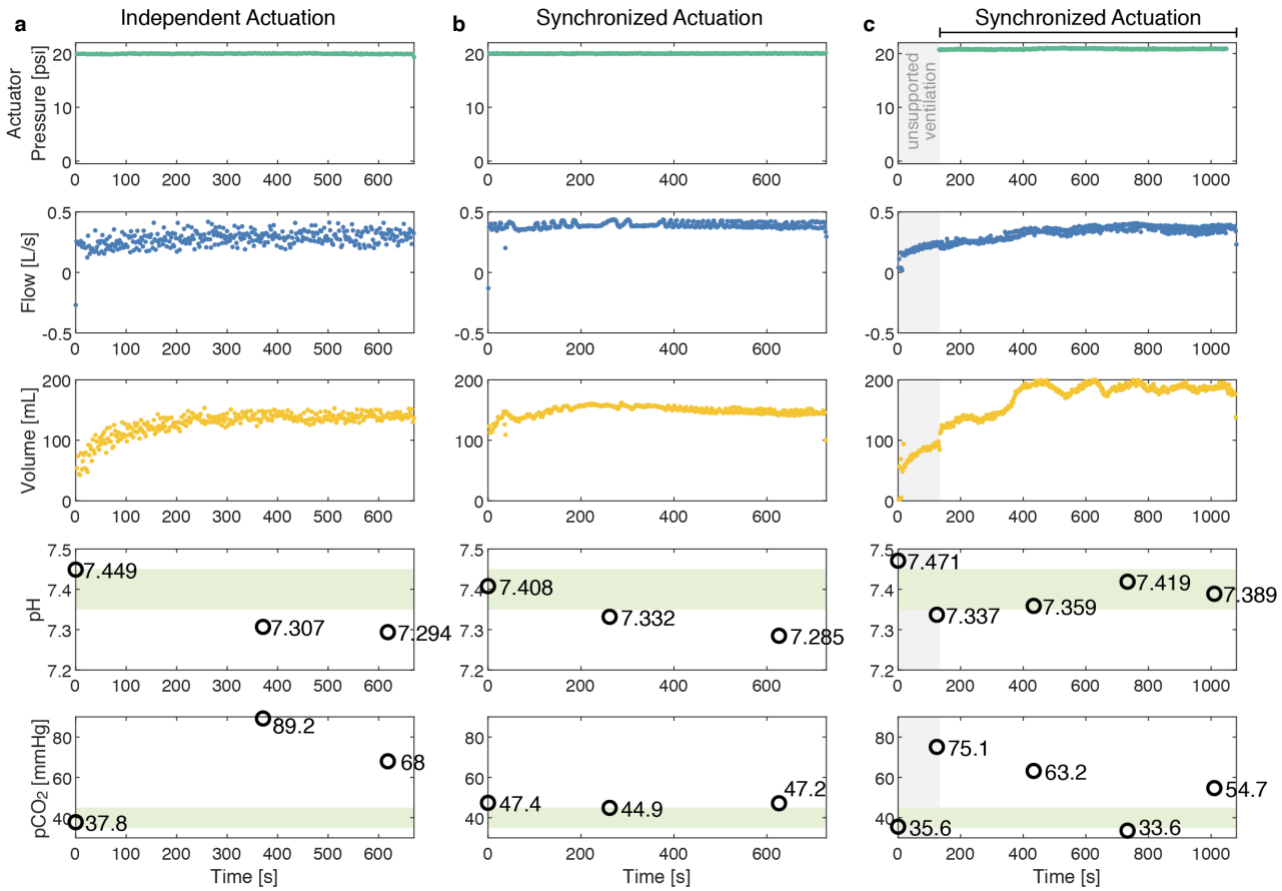

Fig. 5: ABGs taken across distinct respiratory challenges. a, In a respiratory challenge operated with independent actuation, a representative set of peak actuation pressure, peak inspiratory flow, and tidal volumes, and the pH and pCO_2 values from discrete arterial blood gases are shown. **b,** In a respiratory challenge operated with synchronized actuation, a representative set of peak actuation pressure, peak inspiratory flow, and tidal volumes, and the pH and pCO_2 values from discrete arterial blood gases taken during one full respiratory challenge with synchronized actuation. The respiratory challenges depicted in **a,** and **b,** are taken from the same animal. **c,** In another animal, a respiratory challenge began with a 2 minute period of unsupported ventilation and subsequent synchronized actuation. A representative set of peak actuation pressure, peak inspiratory flow, and tidal volumes, and the pH and pCO_2 values from discrete arterial blood gases taken. Gray shading in **c** indicates the period of time where the system is off and respiration is unassisted. In the bottom rows of **a-c**, light green shading indicates the standard range of normal values for each arterial blood gas metric. Complete ABGs can be found in Extended Data Table 1.

Factors in optimizing synchronization.
As seen by the mixed interference in Fig. 4c,h, and the ability of independent actuation to maintain blood gas balance in Fig. 5a, the alignment of the actuation with the underlying respiratory effort will critically determine the constructive versus destructive nature of the interference. In respiratory challenges that had an independent actuation scheme or a poorly synchronized actuation scheme, we found the datasets that provide a natural variation in the timing of the actuation in relationship to the underlying respiratory effort.

Because mechanical respiratory failure exists as a continuous spectrum of loss of function, we looked at the implications of synchronization in different levels of baseline respiratory effort. As seen in Fig. 3, there is variance in the underlying respiratory function between subjects. To simulate a controlled change in the underlying respiratory function within the same subject, we severed the phrenic nerve in some subjects, simulating diaphragm paralysis in combination with the respiratory depression due to the isoflurane (see Methods). Fig. 6 depicts the analysis of aligning the actuator synchronization to the underlying respiratory effort for two respiratory challenges within subject B: (1) the subject with preserved diaphragm function (Fig. 6, left) and (2) the subject with a severed phrenic nerve (Fig. 6, right).

To optimize for maximum inspiratory augmentation, we investigate the relationship of the timing of different waveform features to the resulting tidal volume and peak inspiratory flow of each breath. The high frequency sampling of our data acquisition system (1000 Hz) allows for millisecond temporal resolution. Custom software was written to analyze the actuation pressure, flow, and volume data.

We identify the breath bounds as determined by the local minima in the volume waveform (the locations of V_0), and then finds the time distance between identified waveform features for each individual breath (further details in Methods). Waveform features analyzed include the start of an actuation waveform (P_0), peak inspiratory flow (F_{pk}), the start of inspiration (V_0), the start of expiration (V_{pk}), and others (Fig 6a,b, and Fig. S3).

The distances between features act as different metrics of alignment and elucidate what factors are important to consider in optimizing synchronization. There are many different features and feature distances that can be analyzed. Fig. 6c-f shows the time relationship of the start of expiration to the actuation pressure (V_{pk}-P_0), but other metrics are shown in Fig. S3.

We examine the influence of these time metrics on tidal volume and peak inspiratory flow. We find the most important predictor variables are time metrics related to the start of expiration (V_{pk}). With diaphragm function preserved, there is a weak linear relationship between V_{pk}-P_0 and the peak inspiratory flow ($R^2 = 0.31$, $p<0.001$) (Fig. 6c), and no significant relationship to the tidal volume ($R^2=0.04$, $p=0.001$) (Fig. 6e). However, when the diaphragm function is removed by severing the phrenic nerve, a clear linear relationship emerges between V_{pk}-P_0 and tidal volume ($R^2 = 0.84$, $p<0.001$) (Fig. 6f) and a weaker relationship with peak inspiratory flow ($R^2 = 0.30$, $p<0.001$) (Fig. 6d).

Notably, we do not find these relationships when using the timing between the start of actuation and the start of inspiration (P_0 - V_0) as a metric. There is no linear relationship between P_0-V_0 and the peak inspiratory flow or tidal volume for both the cases with and without diaphragm function (Fig. S4)

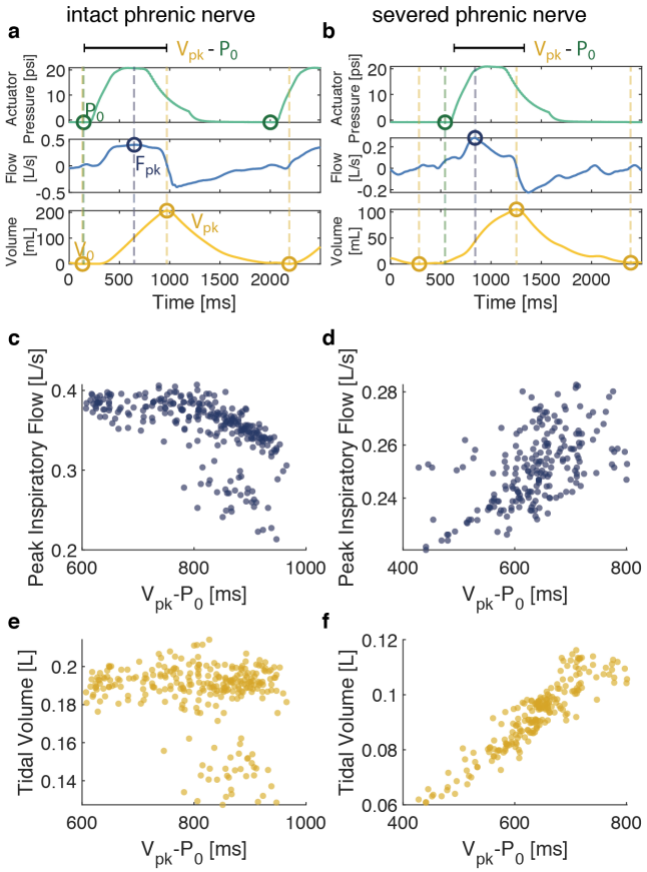

Fig. 6: Effect of the time alignment of actuation and native respiratory effort in two levels of respiratory insufficiency. a,b, Representative actuation pressure, flow, and volume waveforms for a single breath from one respiratory challenge with (**a**) an intact phrenic nerve and one with (**b**) a severed phrenic nerve. Circles mark features that can be identified from the waveforms including the start of actuation (P_0), peak inspiratory flow (F_{pk}), start of the breath (V_0), and peak volume (V_{pk}), and the dashed lines indicate the time point of each feature. **c,d,** A scatter plot of peak inspiratory volume as it relates to the time between V_{pk} and P_0 for one respiratory challenge with an (**c**) intact phrenic nerve and with a (**d**) severed phrenic nerve. **e,f,** A scatter plot of tidal volumes as it relates to the time between V_{pk} and P_0 for one respiratory challenge with an (**e**) intact phrenic nerve and with a (**f**) severed phrenic nerve. All data is taken from the same subject. Each dot represents data from one breath.

Comparing respiratory biomechanics.
To compare the respiratory biomechanics of different modes of respiration and ventilation, pleural pressure (P_{pl}), abdominal pressure (P_{ab}), and transdiaphragmatic pressure (P_{di}; $P_{di} = P_{ab}-P_{pl}$) waveforms are analyzed. Transdiaphragmatic pressure is a metric of diaphragm function[6,30,31]. Pleural pressure and abdominal pressure are approximated by a sensor mounted on a balloon catheter placed in the esophagus and stomach, respectively. As these sensors approximate P_{pl} and P_{ab}, the measurements are interpreted as relative measurements and not absolute measurements (see Methods for information about instrumentation and normalization). When analyzing relative pressure waveforms, the most informative metric is the maximum change in pressure per each breath.

In Fig. 7a-c, we show that across subjects (subject C was not instrumented for pressure measurements, and is therefore not shown), actuator assisted ventilation more closely matches the respiratory biomechanics of spontaneous respiration than in mechanical ventilation. Mechanical ventilation pushes air into the lungs, increasing pleural pressure with inspiration, whereas both actuator assisted ventilation and spontaneous respiration generate a negative pleural pressure to drive airflow. As the diaphragm is passive in mechanical ventilation, we see a negligible change in the abdominal pressure, whereas the caudal movement of the diaphragm in both actuator assisted ventilation and spontaneous respiration increases abdominal pressure.

In the representative waveforms from subject A (Fig. 7d-f)—the case of highest responsiveness as seen per Fig. 3c-e—the actuator assisted ventilation not only more closely resemble that of spontaneous respiration, but also augments all of the pressure waveforms. Actuator assisted ventilation generates more negative changes in pleural pressure, greater increases in abdominal pressure, and ultimately greater increases in transdiaphragmatic pressure per breath.

A graphical technique used to measure work of breathing (WOB) is the Campbell diagram, referencing pleural pressure with lung volume. Using the pressure and volume data from subject A, we generate the pressure-volume (PV) loops of a Campbell diagram (Fig. 7g). Work of breathing is calculated from this PV loop as the internal area between the inspiratory edge of the loop and the passive chest wall compliance derived from the mechanical ventilation PV data. Normal WOB is 0.35-0.7 J/L.[22,32,33] During attenuated spontaneous breathing, the subject's WOB is 0.10 J/L. During actuator assisted ventilation, the assist system shares the WOB and increases the total average WOB to 0.17 J/L, a 66% increase.

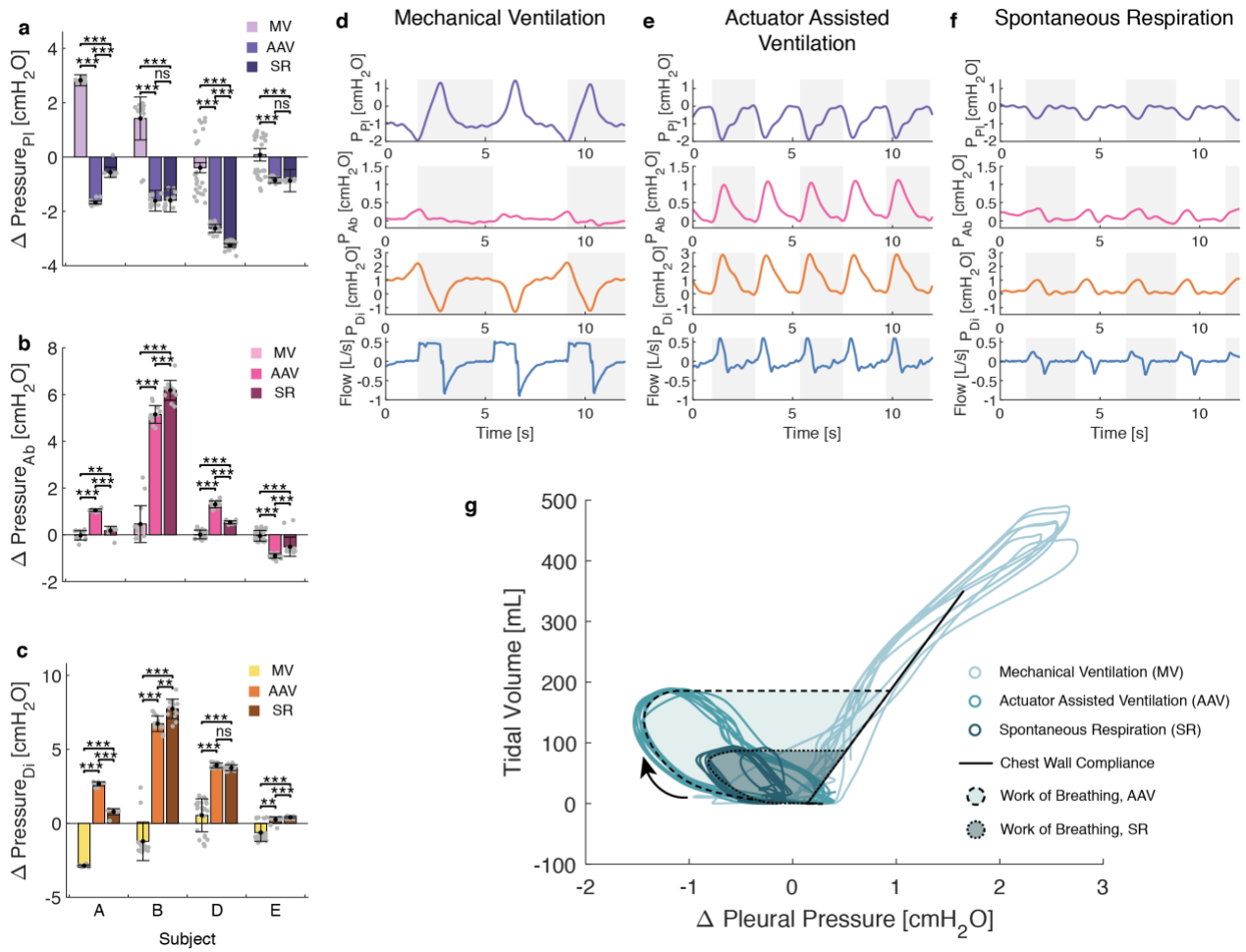

Fig. 7: Comparison of respiratory waveforms. a,b,c, Average change in (**a**) pleural pressure (P_{pl}), (**b**) abdominal pressure (P_{ab}), and (**c**) transdiaphragmatic pressure (P_{di}) per breath under mechanical ventilation (MV), actuator assisted ventilation (AAV), and spontaneous respiration (SR) taken from a representative steady-state segment from one respiratory challenge per subject (*n* = 11-32 breaths). No pressure recordings were taken for subject C or F. Each gray dot represents one breath. **d,e,f,** Representative P_{pl}, P_{ab}, P_{di}, and flow waveforms for (**d**) mechanical ventilation, (**e**) actuator assisted ventilation, and unassisted spontaneous respiration (**f**) from one respiratory challenge from subject A. The alternating grey and white background indicates the bounds of each breath. **g,** Respiratory Campbell diagram plotting the pleural pressure-volume loops for representative breaths from MV, AAV, and SR. The direction of inspiration is indicated by the arrow. The compliance of the passive chest wall derived from the MV is indicated via the solid black line. Shaded regions outlined by dashed lines indicate the area representative of the work of breathing (WOB). In **a-c,** bar plots show mean ± s.d. ns = not significant, **p<0.01, ***p<0.001 using a Wilcoxon rank-sum test.

Discussion

In this work, we use pneumatic soft robotic actuators to support and augment respiration, demonstrating acute augmentation of physiological metrics of respiration, and feasibility as a proof-of-concept device. A set of two McKibben-style PAMs surgically implanted superior to the diaphragm are capable of providing mechanical support to the diaphragm in a large animal model of respiratory insufficiency. We thoroughly characterized the in vitro mechanical properties of the device and investigated its interactions with the respiratory system and the subject, using multimodal metrics to evaluate respiratory function (e.g. tidal volume, inspiratory flow), biomechanics (cavity pressures, WOB), motion (ultrasonography and fluoroscopy), and gas exchange (ABGs).

Contributions

The diaphragm assist system generated substantial augmentation in respiratory function—measured via peak inspiratory flow (a direct metric of inspiratory function), and tidal volume and minute ventilation (metrics of ventilation)—in our most responsive subject. Subject A had the highest change in peak inspiratory pressure, tidal volume, and minute ventilation; the corresponding large augmentation in peak inspiratory pressure indicates that the volume and minute ventilation augmentation are specifically due to the soft robotic actuators augmenting the diaphragm's inspiratory function. Responsiveness to the system varied across subjects.

Variance in responsiveness is likely dependent on a combination of many factors. One factor is the level of preserved respiratory baseline. The weak response in the subject with a relatively high preserved weight-normalized minute ventilation (subject E) suggests that the assist system may have weak augmentation or even a disruptive effect in cases of well-preserved diaphragm function. Other potential factors include precise actuator placement, actuator fit, and anatomical variations.

We showed that synchronization with the native respiratory effort is a critical design element in our system. Synchronous actuation is key to consistent, low-variance respiratory waveforms and tidal volumes. Like standard mechanical ventilation, off-cycle actuation of the actuators can lead to a destructive interference with the underlying respiratory effort, resulting in a poor augmentation and poor blood acid-base balance. In evaluating the effect of synchronization on the system's ability to maintain appropriate gas exchange, we demonstrated that despite generating a similar range of tidal volumes, independent actuation led to an inability to maintain appropriate pCO_2 levels and resulted in respiratory acidosis. Contrastingly, in two trials of well-synchronized actuation, we observed some capacity of the device to maintain and recover baseline pCO_2 levels.

The control system used in this study was a simple but effective first-generation system with many directions for improvement. The synchronization triggered from airway flow–which is also the metric used by gold standard clinical ventilatory support options for triggering–but flow is also the most downstream signal in neuro-ventilatory coupling. The downstream nature of the signal is a potential source of delays and asynchrony[34]. In order to achieve consistent assistance from breath to breath, the synchronization must be optimized for the alignment that maximizes constructive interference. The system relied on a manually titrated threshold set for the flow sensor data. It is designed to be triggered at the start of an inspiratory flow effort, which is related to V_0. However, the manual nature of the system meant that if the threshold was set too low, noise in the flow signal could cause pre-emptive or false triggering (as evidenced by the negative values for P_0-V_0). Our alignment analysis

reveals two important considerations for improvements towards this goal. The first consideration is that the influence of alignment changes with the degree of preserved respiratory function, as seen with the difference in results between the intact and the severed phrenic nerve. When the phrenic nerve is severed, all diaphragm motion is governed by the actuators, and misaligned actuation with the remaining native respiratory effort—expansion of the ribcage—results in more consequential destructive interference. Whereas when the phrenic nerve is intact, the net diaphragm motion results from a combination of native diaphragm function and the effect of the actuators, because the actuators only operate along 2 discrete lines on the diaphragm. The contraction of the rest of the native diaphragm motion is still synchronized with the ribcage motion, so the effects of misalignment are less apparent. This implies that optimal alignment parameters may be different for different disease states and the control system will need to be dynamic and adaptive to changes in respiratory function, even within the same patient. The second consideration is that the actuation curve's relationship to the beginning of expiration (V_{pk}) is more influential than the relationship to the beginning of inspiration (V_0). This implies that an updated system should trigger from a signal related to expiration as opposed to the beginning of inspiration. Some neuromuscular signals, like the electrical activity of the diaphragm (Edi), contain detailed information about both inspiration and expiration times[35,36]. Edi amplitude is also proportional to the neural drive, as well as the degree of contraction of the diaphragmatic muscle, therefore opening up the possibility of adaptive control. Triggering from Edi measured at the esophageal level via a feeding tube[37] may be warranted to improve mechanical ventilation. This method, known as neurally adjusted ventilatory assist, is available in the clinical setting with mechanical ventilation and may improve respiratory weaning of patients that are challenging to wean[36]. The same principle could be applied to our diaphragm assist system; using a more upstream signal with greater information on the native respiratory effort would allow for a more robust control system.

Overall, we show that the strategy to augment the native function of the diaphragm with soft robotics acts as a form of negative pressure ventilation by driving ventilation through the generation of a negative pressure in the thoracic cavity. Our diaphragm assist system is biomechanically similar to that of spontaneous breathing, sharing a substantial portion of the work of breathing in our best responding subject. By functioning as an assist device—as opposed to completely overtaking breathing—our system has the potential to be compatible with voluntary use of the diaphragm. Maneuvers such as voluntary deep breaths or drinking through a straw—abilities related to patient autonomy and quality of life—can be preserved with this implantable ventilator strategy. Additionally, in contrast to current modes of mechanical ventilation, recapitulation of native biomechanics, as shown with this system, can avoid the deleterious effects that arise secondary to the use of positive pressure ventilation, such as barotrauma[38,39] or hemodynamic changes in patients with concurrent cardiac pathologies[40,41].

Overall limitations

In this study, we demonstrate the foundational work towards a soft robotic implantable ventilator. Translationally, there are many hurdles to overcome between the proof-of-concept state presented here and the ultimately envisioned system, and we discuss them in the subsequent text.

Given that we saw variable responsiveness to the device across subjects, additional studies are needed to understand what factors in system design and implantation can replicate high responsiveness. Our

system could generate the low end of acceptable minute ventilations but relied on high respiratory rates to do so. Given the presence of dead space, low tidal volumes result in less alveolar ventilation than if the same minute ventilation achieved with higher tidal volumes and a lower respiratory rate. A core goal of the next generation system is to further improve the tidal volume augmentation, which will need to be achieved through both actuator design and control system development.

Here, we used the classic McKibben actuator; a more application-specific or customized actuator type may allow for further increases in tidal volumes in future work. Other factors in actuator design, such as the number, layout, and positioning of actuators, will also be critical. We demonstrated tunability of assist by controlling pressurization, but an updated design will require finer characterization. Synchronization is critical to device performance, and thus future work lies in building a next generation control system; this includes creating a system that is cognizant of the beginning of expiration as opposed to inspiration, an automated control system that removes the error of manual titration, and further investigation of dynamic actuation curves. An ideal next generation control system aims to trigger from a more upstream neural signal–such as the electrical activity of the diaphragm–to provide an earlier signal that enables an advanced control system to optimize synchronization, removing delays and asynchrony. Neural triggering via implanted electrodes would also untether the current system from the flow instrumentation, freeing the patient from interventions at the mouth or trachea. To fully realize untethering from bulky machines–like standard mechanical ventilators–the external components that control and power the system require miniaturization. Future work will aim to eventually miniaturize the system to the scale of a small backpack–one that could be worn by the patient or attached to a belt or an electric wheelchair. The process of miniaturization and portability has proved to be possible in similar complex devices, such as ventricular assist devices (e.g. Thoratec HeartMate III) or total artificial hearts (e.g. Syncardia TAH, Carmat Aeson)[42–45].

Towards clinical translation

Envisioning a translation to the clinical field, the following considerations might help to optimize the management and pave the way to human application. The diseases leading to chronic diaphragmatic dysfunction are numerous and feature very different pathophysiologies. Therefore, a thorough understanding of the underlying pathology as well as its specificity are critically needed to help optimize the management and anticipate complications[46]. Moreover, patient selection and indication will need to be clearly defined, in order to select the patients who will benefit from this therapy the most. Here, we present a generalized mechanical strategy for diaphragm support, but the parameters of actuator design or actuation control will need to be optimized and specialized per the needs of a given pathology as well as individual patient anatomy.

Owing to the complexity of the procedure, a multidisciplinary team highly trained in advanced thoracic surgery is required to build expertise and develop this technology, ideally in a high-volume center[47]. Technological improvement is required to provide the least invasive approach of implantation. In this regard, a thoracoscopic route might be beneficial and will be the subject of future work. Given the invasive nature of implantable devices, the diaphragm assist platform is targeted towards patients with chronic-to-permanent ventilator dependence. We recognize that surgery in patients suffering severe diaphragm dysfunction causing respiratory failure can carry a high morbidity and mortality. Peri-operative complications can be numerous; one of the most feared is the worsening of the pulmonary

status, which may itself precipitate the need for long-term ventilation[48]. Nevertheless, it has been well demonstrated that complex thoracic surgery is feasible even in very frail patients. Lung transplantation for terminal respiratory disease[49] is one of the most striking examples. Thus, surgery could still be considered in a suitable target population that would ultimately benefit from this mechanical augmentation of diaphragm function, such as a range of neuromuscular disorders. The concept of diaphragm assist is in itself a means of preventing further complications from chronic respiratory failure and preserving key aspects of quality of life-like speech and mobility.

Due to the focus on feasibility, we acknowledge that there are limitations in these acute studies from the lens of regulatory approval and clinical translation. We do not study device biocompatibility or long-term device operation. The device was constructed from types of polymers that are already used in established medical devices[50–53], such as poly(ethylene terephthalate) (PET) and polyurethanes (See Supplemental Information). Because our device focuses on mechanical interaction, as opposed to biochemical interactions with the body, the materials used in the device can easily be substituted with regulatory-approved materials in future iterations. With improved performance and stability, future long-term studies will need to investigate the long-term effects of the system including tissue remodeling and the ability to provide full-time respiratory support.

Although this technology requires further advancements in the net tidal volumes it can generate before it can fully match the ventilation capacity of a current mechanical ventilator, it is the first study to report the ability to rescue ventilation with an implantable ventilator. We envision further translational potential of this technology when combined with the development of smaller and more portable pneumatic energy sources[54,55] as the field of soft robotics advances. With the integration of a portable pump and control system in the future, this technology could provide an additional level of patient autonomy via increased mobility. Motivated by the encouraging results of this study, we believe this technology, with optimized design, has the potential to provide a radically different ventilation technology that preserves key metrics of quality of life for people with end-stage mechanical respiratory failure.

Methods

Study design.

There were two main objectives of our study. First, we sought to demonstrate the proof-of-concept capability to augment ventilation via implanted soft robotic actuators in an animal model of respiratory muscle weakness. To evaluate ventilation metrics, we measured spirometric flow and volume. Second, we aimed to demonstrate that this soft robotic strategy replicates more native respiratory biomechanics than standard mechanical ventilation. To evaluate the respiratory biomechanics, we evaluated the respiratory pressure data along with the spirometry data.

In order to evaluate the system performance under varying conditions within a single animal, a series of respiratory challenges were performed. Prior to the first and between each subsequent respiratory challenge, volume control mechanical ventilation operated through the facility's Drager Tiro ventilator (Drägerwerk AG, Lübeck, Germany) was used to maintain the animal's ventilation needs and recover from respiratory challenges if needed. Arterial blood gases were taken to validate normal baseline respiratory status prior to each challenge. Each respiratory challenge was initiated by switching the ventilator to a manual mode of ventilation. Data for a mix of unsupported ventilation and actuator-supported ventilation was collected. Vital signs and respiratory status were monitored. For experiments with uninterrupted trials, ABGs were collected at 2 or 5-minute intervals during the challenge.

Fabrication and characterization of pneumatic artificial muscles. The actuators were a modified version of the PAM actuators previously described in Roche, E.T. et al[7], and Payne, C., et al[9] . Specifically, McKibben pneumatic artificial muscles were fabricated according to the protocol detailed in the Supplementary Methods. Actuator dimensions were selected to fit the anatomical needs of the 30-40 kg swine. They consist of a thermoplastic elastomer bladder (Stretchlon 200, FibreGlast Developments Corp.), a thermoplastic polyurethane tubing (1/8" Tubing, 5648K226, McMaster, Inc) and an expandable braided mesh (PTO0.25BK, TechFlex, Inc.). Prior to use *in vivo*, actuators were fatigue tested to a pressurization of 20 psi for >1000 cycles on the benchtop. Mechanical characterization was performed on an Instron 5499 Universal Testing System (Instron Corp, Norwood, MA, USA).

Actuator characterization was conducted both *in vitro* and *in vivo*. For the *in vitro* characterization, actuator performance was measured via Instron testing. Classic tensile testing was conducted to measure the contractile force. A modified flexural bend setup (Fig. S5) was used to measure the perpendicular force applied to the diaphragm via arclength shortening. For the in vivo characterization, performance of the diaphragm assist system was evaluated through the diaphragm displacement (via ultrasonography) and the functional metrics (tidal volume, Campbell diagram) (Extended Data Fig. 1 and 2). Different pressurization shapes and levels were input into the actuator (Extended Data Fig. 1 and 2) and the resulting behavior was measured. Further details can be found in the Supplementary Information.

Live animal studies.

All studies were conducted according to protocol #19-05-3907 approved by the Boston Children's Hospital (BCH) Institutional Animal Care and Use Committee (IACUC) policy.

Procedures were carried out at Boston Children's Hospital in accordance with BCH IACUC under protocol #19-05-3907 and MIT IACUC under protocol #0118-006-21. Protocol reviews were conducted in accordance with the standards outlined in the National Research Council's Guide for the Care and Use of Laboratory Animals and BCH's Animal Welfare Assurance.

Female Yorkshire 30-40kg swine were sourced from Parson's Farm (Hadley, MA, USA). We used a total of twelve swine during the development and testing of our system, and we present data from nine swine in the manuscript. Different subsets of subjects were used for the experimental investigations reported; not all subjects were used in every experimental investigation. Animals were acclimated and cared for according to standard facility protocols. Each experiment was conducted under 2-3% isoflurane anesthesia, titrated to each animal to maintain a stable anesthetic plane. Anesthesia and mechanical ventilation were controlled through the facility's Drager Tiro ventilator (Drägerwerk AG, Lübeck, Germany). Vital signs were monitored via a SurgiVet monitor (Smiths Medical, Inc., Minneapolis, MN, USA). After completing the study and acquiring the data, animals were euthanized using Fatal-Plus Solution (Vortech Pharmaceuticals, Dearborn, Michigan) at a dose of 110 mg/kg/body weight.

Surgical procedure.
After induction of anesthesia, the animal was intubated and placed on mechanical ventilation. A transesophageal EKG catheter was placed to monitor the heart rate. A carotid arterial sheath and jugular venous line were placed using cut-down technique for animal systemic and central venous pressures monitoring respectively. Two balloons were placed, one in the esophagus and one in the stomach for pressure monitoring. A Foley catheter was placed for urine output monitoring. Following that, the chest cavity was accessed through midline sternotomy. Next, we opened both pleural cavities and placed one soft actuator along the diaphragm curvature on each cavity. The anterior portion is attached to the sternum and the posterior attachment is made to the lowest posterior rib in the most medial position that can be achieved without disrupting the region of the major arteries and veins, esophagus, and spine. To do this, we passed each actuator posteriorly at lowest intercostal space to outside the chest cavity and fixed it to the skin using sutures. Then, we fixed the other end to the sternum using sutures and we passed the actuation lines through separate opening through the skin. Next, we approximated the sternum using sternal wires and close the subcutaneous layers and the skin in layers using sutures. After the sternotomy was closed, the negative pressure in the thoracic cavity was restored via chest tube, and the respiratory challenges were conducted with a closed chest.

Simulating varying levels of respiratory function.
In order to simulate varying levels of respiratory functions, two animal models of respiratory muscle weakness were used. The first method relied on the respiratory depressive effects of isoflurane. Isoflurane levels were held between 2-3% and titrated to a stable plane of anesthesia while still maintaining a depressed but non-zero level of spontaneous respiration during respiratory challenges. The second method modeled diaphragm paralysis via mechanically severing both the left and right phrenic nerves. This model is still conducted under the setting of the isoflurane, and thus combines the effects of the isoflurane and severed phrenic nerve and represents a more severe model of respiratory model weakness.

Data acquisition.
The biomedical sensors and instrumentation data were input into a PowerLab 35 series (PL3516, ADInstruments, Dunedin, New Zealand) high performance data acquisition system with a 1000Hz sampling frequency for all channels. During the experiments, data was monitored live via LabChart software (ADInstruments, Dunedin, New Zealand). After the experiements, data was exported into and processed in MATLAB (MathWorks, Portola Valley, CA, USA).

Spirometry instrumentation.
An analog spirometer (Gas Flow Sensor, ES Systems, Filothei-Psychiko, Greece) was placed in line between the ventilator Y-tubing and the endotracheal tube. Analog data was input into the PowerLab. The data was converted from mass flow to volumetric flow according to manufacturer specifications

Respiratory pressure instrumentation and measurement.
Pleural pressure and abdominal pressure were measured via an esophageal balloon catheter (Cooper Surgical, Trumbull, CT, USA) placed in the esophagus and stomach respectively, each connected to a pressure transducer (PRESS-S-000, PendoTech, Princeton, NJ, USA).

Respiratory pressure data was normalized in the MATLAB post-processing. For a given segment of interest, the average of the pressure reading at the breath bounds was set to zero, to allow the analysis to show the change in pressure over the course of one breath.

Ultrasonography.
Ultrasonography (US), a non-invasive, non-ionizing imaging method, was used to investigate the interactions of the device with the diaphragm. US can be used to assess diaphragm displacement and dysfunction[25]. More precisely, it allows a direct two-dimensional visualization of the diaphragm, permitting a quantification of its motion and function, and serves as an ideal tool to assess the interaction of the device with the diaphragm. A Philips iE33 (Philips Healthcare, Andover, MA, USA) echography machine was used with the X7-2 transducer (Philips Healthcare, Andover, MA, USA). A 2-dimensional image (so-called B-mode, Brightness) of the diaphragm and the device was obtained by placing the probe in the right subcostal space, pointing in the cranial direction. To quantify the motion of the device and the diaphragm, M-mode was used.

Control system design and instrumentation.
Our group has built a custom electropneumatic control system utilizing electropneumatic pressure regulators and valves (SMC Pneumatics, SMC Corp, Tokyo, Japan) controlled by a custom software described in Horvath, Hu et al[56]. The software is designed to allow custom pressure waveforms to be input. The control system can generate a desired waveform via an analog input to the electopneumatic regulators. The nominal peak pressure for all waveforms was 20 psi. The regulators also output an analog signal of the actual pressure waveform; this data is input into the PowerLab system.

Independent and synchronized actuation.
The custom control system is capable of generating a manual timing set to a frequency of actuation that is initiated by user input. This set timing initiates the custom pressure waveform programmed into the system. This timing is independent of the subject's native breathing.

In order to implement synchronization in our system, the Fast Response Output add-on for LabChart (ADInstruments, Dunedin, New Zealand). Analog spirometry flow data was used as the input channel. Voltage and hysteresis settings were manually titrated between a voltage range equivalent to 0.01 L/s to 0.07 L/s and a hysteresis range between 2-5% during every respiratory trial to achieve qualitatively good synchronization, as visually recognized by the homogeneity of the real-time flow and volume waveforms. The digital output channel on the PowerLab was used to send a trigger pulse to a digital input channel in the microcontroller of the custom control system described above.

Statistical analysis

Statistical tests were conducted as described in the respective figure captions for Fig. 3, 4, 7, and Extended Data Fig. 1 and 2. For Fig. 3c,d and Fig. 7a-c, two-sided Wilcoxon rank-sum analyses were conducted in MATLAB (MathWorks, Portola Valley, CA, USA) via the “ranksum” function. Fig. 4e,f depicts two sets of statistical tests. A two-sided Welch’s t-test without assuming equal variances was conducted in order to compare the means of the populations via the “ttest2” function in MATLAB with an “unequal” variance type specification. Additionally, a 2-sample F-test for equal variances was conducted to compare and confirm unequal variances via the “vartest2” function in MATLAB. For the Extended Data Fig. 1 and 2, two-sided t-tests were conducted via the “ttest2” function in MATLAB.

Data availability

The datasets generated during and/or analyzed during the current study are available from the corresponding author on reasonable request.

References

1. Hutchinson, D. & Whyte, K. Neuromuscular disease and respiratory failure. *Pract. Neurol.* **8**, 229–237 (2008).
2. Groth, S. S. & Andrade, R. S. Diaphragm Plication for Eventration or Paralysis: A Review of the Literature. *ATS* **89**, S2146–S2150 (2010).
3. Col Henry Tripp, L. F. & Col W Randolph Bolton, L. J. Phrenic Nerve Injury Following Cardiac Surgery: A Review. *J Card Surg* **73**, 218–223 (1998).
4. Leung, D. G. & Wagner, K. R. Therapeutic advances in muscular dystrophy. *Ann. Neurol.* **74**, 404–411 (2013).
5. Kurtzke, J. F. Epidemiology of amyotrophic lateral sclerosis. *Adv. Neurol.* **36**, 281–302 (1982).
6. Caruso, P. *et al.* Diagnostic methods to assess inspiratory and expiratory muscle strength. *J. Bras. Pneumol.* **41**, 110–123 (2015).
7. Roche, E. T. *et al.* Soft robotic sleeve supports heart function. *Sci. Transl. Med.* **9**, 1–12 (2017).
8. Payne, C. J. *et al.* Soft robotic ventricular assist device with septal bracing for therapy of heart failure. *Sci. Robot.* **2**, eaan6736 (2017).
9. Payne, C. J. *et al.* An Implantable Extracardiac Soft Robotic Device for the Failing Heart: Mechanical Coupling and Synchronization. *Soft Robot.* **4**, 241–250 (2017).
10. Saeed, M. Y. *et al.* Dynamic Augmentation of Left Ventricle and Mitral Valve Function With an Implantable Soft Robotic Device. *Basic to Transl. Sci.* **5**, 229–242 (2020).
11. Hong, Y. J., Jeong, H., Cho, K. W., Lu, N. & Kim, D. H. Wearable and Implantable Devices for Cardiovascular Healthcare: from Monitoring to Therapy Based on Flexible and Stretchable Electronics. *Adv. Funct. Mater.* **29**, 1808247 (2019).
12. Bashkin, J. S., Heim, J. & Prahlad, H. Medical Device Applications of Dielectric Elastomer Based Artificial Muscles. in *Medical Device Materials IV: Proceedings of the 2007 Materials and Processes for Medical Devices Conference* (2007).
13. Cianchetti, M., Laschi, C., Menciassi, A. & Dario, P. Biomedical applications of soft robotics. *Nat. Rev. Mater. 2018 36* **3**, 143–153 (2018).
14. Damian, D. D. *et al.* In vivo tissue regeneration with robotic implants. *Sci. Robot.* **3**, (2018).
15. Iacovacci, V. *et al.* A fully implantable device for intraperitoneal drug delivery refilled by ingestible capsules. *Sci. Robot.* **6**, 3328 (2021).
16. Dolan, E. B. *et al.* An actuatable soft reservoir modulates host foreign body response. *Sci. Robot.* **4**, (2019).
17. Menciassi, A. & Iacovacci, V. Implantable biorobotic organs. *APL Bioeng.* **4**, 1–4 (2020).
18. Perez-Guagnelli, E. *et al.* Characterization, Simulation and Control of a Soft Helical Pneumatic Implantable Robot for Tissue Regeneration. *IEEE Trans. Med. Robot. Bionics* **2**, 94–103 (2020).
19. Pane, S., Mazzocchi, T., Iacovacci, V., Ricotti, L. & Menciassi, A. Smart implantable artificial bladder: An integrated design for organ replacement. *IEEE Trans. Biomed. Eng.* **68**, 2088–2097 (2021).
20. Amiri Moghadam, A. A. *et al.* Using Soft Robotic Technology to Fabricate a Proof-of-Concept Transcatheter Tricuspid Valve Replacement (TTVR) Device. *Adv. Mater. Technol.* **4**, (2019).
21. Bashkin, J. S., Kornbluh, R., Prahlad, H. & Wong-Foy, A. Biomedical Applications of Dielectric Elastomer Actuators. in *Biomedical Applications of Electroactive Polymer Actuators* (eds. Carpi, F. & Smela, E.) 395–410 (John Wiley & Sons, Ltd, 2009).
22. de Vries, H., Jonkman, A., Shi, Z.-H., Man, A. S. & Heunks, L. Assessing breathing effort in mechanical ventilation: physiology and clinical implications. *Ann. Transl. Med.* **6**, 387–387 (2018).

23. Daerden, F. & Lefeber, D. Pneumatic Artificial Muscles: actuators for robotics and automation. *Eur. J. Mech. Environ. Eng.* (2002).
24. Chou, C. P. & Hannaford, B. Measurement and modeling of McKibben pneumatic artificial muscles. *IEEE Trans. Robot. Autom.* **12**, 90–102 (1996).
25. Vetrugno, L. *et al.* Ultrasound Imaging for Diaphragm Dysfunction: A Narrative Literature Review. *J. Cardiothorac. Vasc. Anesth.* **33**, 2525–2536 (2019).
26. Cohen, I. T., Deutsch, N. & Motoyama, E. K. Induction, Maintenance, and Recovery. *Smith's Anesth. Infants Child.* 365–394 (2011). doi:10.1016/B978-0-323-06612-9.00013-4
27. Hannon, J. P., Bossone, C. A. & Wade, C. E. Normal Physiological Values for Conscious Pigs Used in Biomedical Research. (1989).
28. Thille, A. W., Rodriguez, P., Cabello, B., Lellouche, F. & Brochard, L. Patient-ventilator asynchrony during assisted mechanical ventilation. *Intensive Care Med. 2006 3210* **32**, 1515–1522 (2006).
29. Bailey, J. M. Management of Patient-Ventilator Asynchrony. *Anesthesiology* **134**, 629–636 (2021).
30. Davis, J. N., Goldman, M., Loh, L. & Casson, M. Diaphragm function and alveolar hypoventilation. *Q. J. Med.* **45**, 87–100 (1976).
31. Panitch, H. B. The Pathophysiology of Respiratory Impairment in Pediatric Neuromuscular Diseases. *Pediatrics* **123**, S215–S218 (2009).
32. Hess, D. R. Respiratory mechanics in mechanically ventilated patients. *Respir. Care* **59**, 1773–1794 (2014).
33. Mancebo, J. *et al.* Comparative effects of pressure support ventilation and intermittent positive pressure breathing (IPPB) in non-intubated healthy subjects. *Eur. Respir. J.* **8**, (1995).
34. Dres, M., Rittayamai, N. & Brochard, L. Monitoring patient-ventilator asynchrony. *Curr. Opin. Crit. Care* **22**, 246–253 (2016).
35. Parthasarathy, S., Jubran, A. & Tobin, M. J. Assessment of neural inspiratory time in ventilator-supported patients. *Am. J. Respir. Crit. Care Med.* **162**, 546–552 (2000).
36. Yuan, X. *et al.* Neurally adjusted ventilatory assist as a weaning mode for adults with invasive mechanical ventilation: a systematic review and meta-analysis. *Crit. Care* **25**, 1–11 (2021).
37. Sinderby, C., Beck, J., Spahija, J., Weinberg, J. & Grassino, A. Voluntary activation of the human diaphragm in health and disease.
38. Boussarsar, M. *et al.* Relationship between ventilatory settings and barotrauma in the acute respiratory distress syndrome. *Intensive Care Med. 2002 284* **28**, 406–413 (2002).
39. Ioannidis, G. *et al.* Barotrauma and pneumothorax. *J. Thorac. Dis.* **7**, S38 (2015).
40. Thomson, A. The role of negative pressure ventilation. *Arch. Dis. Child.* **77**, 454–458 (1997).
41. Shekerdemian, L. S. *et al.* Cardiopulmonary interactions in healthy children and children after simple cardiac surgery: the effects of positive and negative pressure ventilation. *Heart* **78**, 587–593 (1997).
42. Han, J. & Trumble, D. R. Cardiac assist devices: Early concepts, current technologies, and future innovations. *Bioengineering* **6**, (2019).
43. Thunberg, C. A., Gaitan, B. D., Arabia, F. A., Cole, D. J. & Grigore, A. M. Ventricular Assist Devices Today and Tomorrow. *J. Cardiothorac. Vasc. Anesth.* **24**, 656–680 (2010).
44. Carrier, M. *et al.* Outcomes after heart transplantation and total artificial heart implantation: A multicenter study. *J. Hear. Lung Transplant.* **40**, 220–228 (2021).
45. Latrémouille, C. *et al.* A bioprosthetic total artificial heart for end-stage heart failure: Results from a pilot study. *J Hear. Lung Transpl.* **37**, 33–37 (2017).
46. Brambrink, A. M. & Kirsch, J. R. Perioperative Care of Patients with Neuromuscular Disease and

Dysfunction. *Anesthesiol. Clin.* **25**, 483–509 (2007).
47. Darling, G. E. Regionalization in thoracic surgery: The importance of the team. *J. Thorac. Cardiovasc. Surg.* **161**, 323–329 (2021).
48. Katz, J. A. & Murphy, G. S. Anesthetic consideration for neuromuscular diseases. *Curr. Opin. Anaesthesiol.* **30**, 435–440 (2017).
49. Chambers, D. C. *et al.* The International Thoracic Organ Transplant Registry of the International Society for Heart and Lung Transplantation: Thirty-eighth adult lung transplantation report — 2021; Focus on recipient characteristics. *J. Hear. Lung Transplant.* **40**, 1060–1072 (2021).
50. Subramaniam, A. & Sethuraman, S. Biomedical Applications of Nondegradable Polymers. *Nat. Synth. Biomed. Polym.* 301–308 (2014). doi:10.1016/B978-0-12-396983-5.00019-3
51. Ratner, B. D. Polymeric Implants. *Polym. Sci. A Compr. Ref. 10 Vol. Set* **9**, 397–411 (2012).
52. Wang, W. & Wang, C. Polyurethane for biomedical applications: A review of recent developments. *Des. Manuf. Med. Devices* 115–151 (2012). doi:10.1533/9781908818188.115
53. Rahimi, A. & Mashak, A. Plastics, Rubber and Composites Review on rubbers in medicine: natural, silicone and polyurethane rubbers A Rahimi & A Mashak Review on rubbers in medicine: natural, silicone and polyurethane rubbers. *Plast. Rubber Compos.* **42**, 223–230 (2013).
54. Wehner, M. *et al.* An integrated design and fabrication strategy for entirely soft, autonomous robots. *Nat. 2016 5367617* **536**, 451–455 (2016).
55. Zhang, J. *et al.* Robotic Artificial Muscles: Current Progress and Future Perspectives. *IEEE Trans. Robot.* **35**, 761–781 (2019).
56. Horvath, M. A. *et al.* An organosynthetic soft robotic respiratory simulator. *APL Bioeng.* **4**, 026108 (2020).

Extended Data

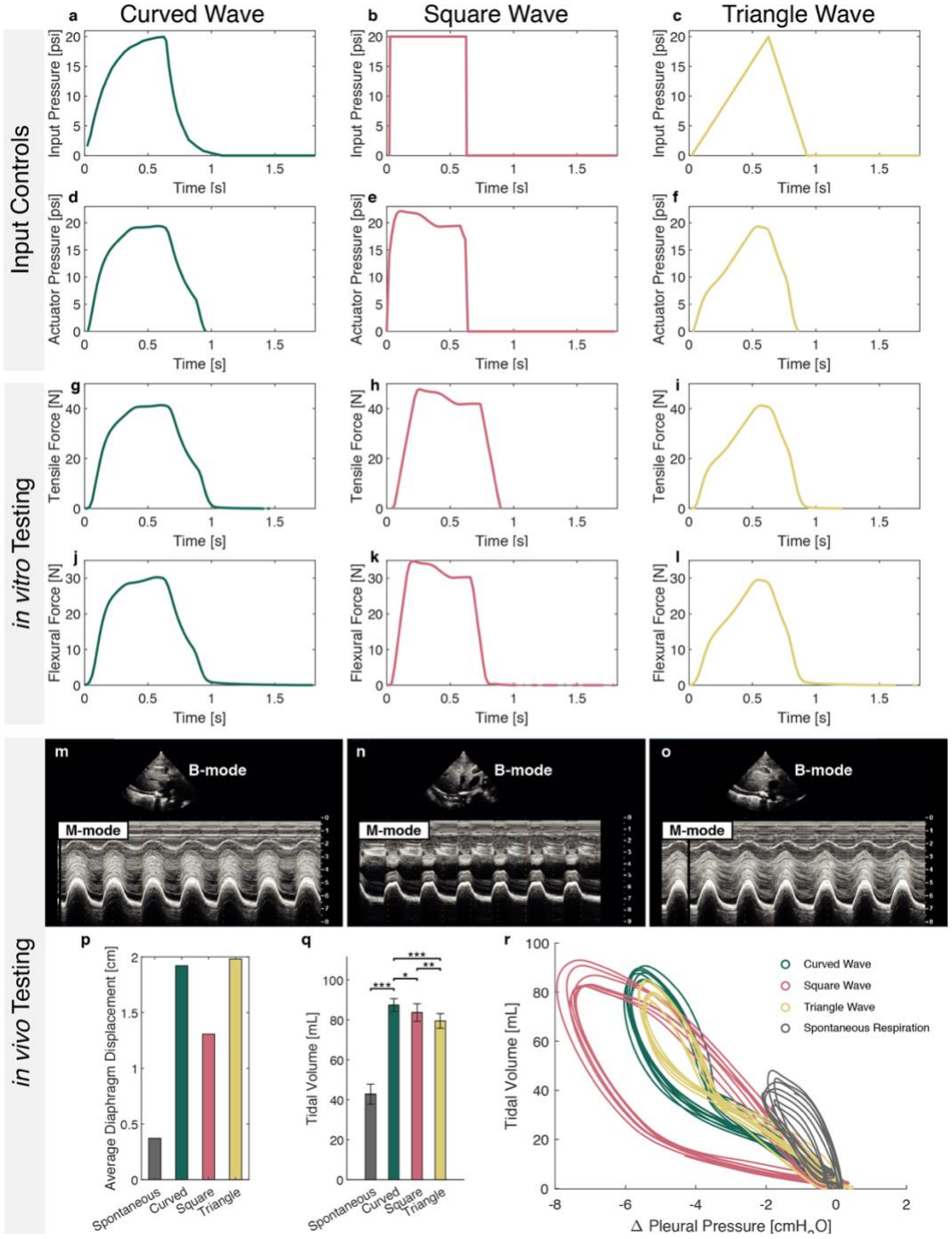

Extended Data Fig. 1. Controlling actuation via different pneumatic waveforms. Input waveforms of a (**a**) curved, (**b**) square, and (**c**) triangle shape can be programmed into the custom-built control system. The effective output pressure of the electropneumatic regulator for the (**d**) curved, (**e**) square, and (**f**) triangle shape drives actuation. The PAM actuation forces were characterized for different waveforms *in vitro* on a classic Instron tensile test setup (**g**,**h**,**i**) and our modified flexural test setup (**j**,**k**,**l**) (depicted in Fig. S5). Input waveforms of a (**m**) curved, (**n**) square, and (**o**) triangle shape generate different shapes of diaphragm displacement as visualized via M-mode ultrasound. (**p**) Average diaphragm displacement from **m**,**n**,**o**. (**q**) Average tidal volume and (**r**) respiratory Campbell diagram plotting the pleural pressure-volume loops for representative breaths from different waveform shapes. Significance is indicated by *p<0.05,**p<0.01,***p<0.001 for a two-sample t test.

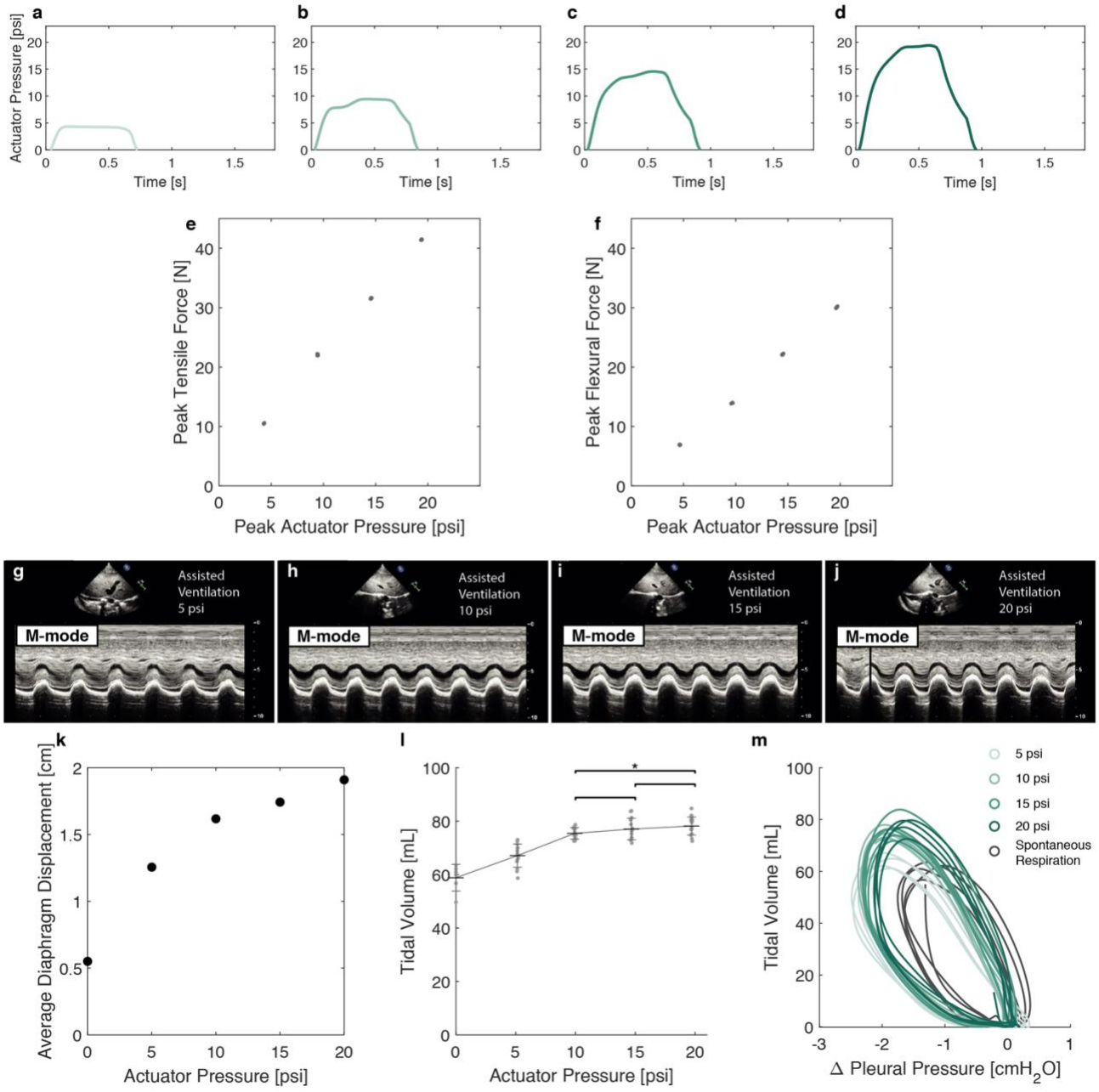

Extended Data Fig. 2. Tuning actuation depth via level of pressurization. The actuator pressure profile for a curved waveform scaled to have a peak nominal pressure of (**a**) 5 psi, (**b**) 10 psi, (**c**) 15 psi, (**d**) 20 psi. The peak forced generated by different levels of actuation were characterized *in vitro* on a (**e**) classic Instron tensile test setup and (**f**) our modified flexural test setup (depicted in Fig. S5).Diaphragm displacement generated by actuations of (**g**) 5 psi, (**h**) 10 psi, (**i**) 15 psi, (**j**) 20 psi visualized via M-mode ultrasound. (**k**) The average diaphragm displacement per breath from one sample subject via M-mode ultrasound. (**l**) Tidal volume achieved via different levels of pressurization from one sample subject. Significance is indicated by *p<0.05 for a two-sample t test. (**m**) Respiratory Campbell diagram plotting the pleural pressure-volume loops for representative breaths from different levels of actuation.

a

Time [s]	0	370	618
pH	7.449	7.307	7.294
pCO2 [mmHg]	37.8	89.2	68
HCO3 [mmol/l]	26.4	45	33.3
pO2 [mmHg]	313.4	228.2	189
sO2 [%]	99	100	99

b

Time [s]	0	262	626
pH	7.408	7.332	7.285
pCO2 [mmHg]	47.4	44.9	47.2
HCO3 [mmol/l]	30.2	24	22.6
pO2 [mmHg]	246	217.9	158.2
sO2 [%]	99	100	100

c

Time [s]	0	124	433	732	1010
pH	7.471	7.337	7.359	7.419	7.389
pCO2 [mmHg]	35.6	75.1	63.2	33.6	54.7
HCO3 [mmol/l]	26.2	40.6	36	21.9	33.4
pO2 [mmHg]	256.6	233.1	292.4	232.7	272.2
sO2 [%]	99	99	100	100	99

Extended Data Table 1. Full arterial blood gas results. Arterial blood gas results for the respiratory challenges reported in Fig. 5. Here, Table **1 a,b,c** corresponds with Fig. 5a,b,c respectively.

List of Supplementary Materials

Supplementary Information

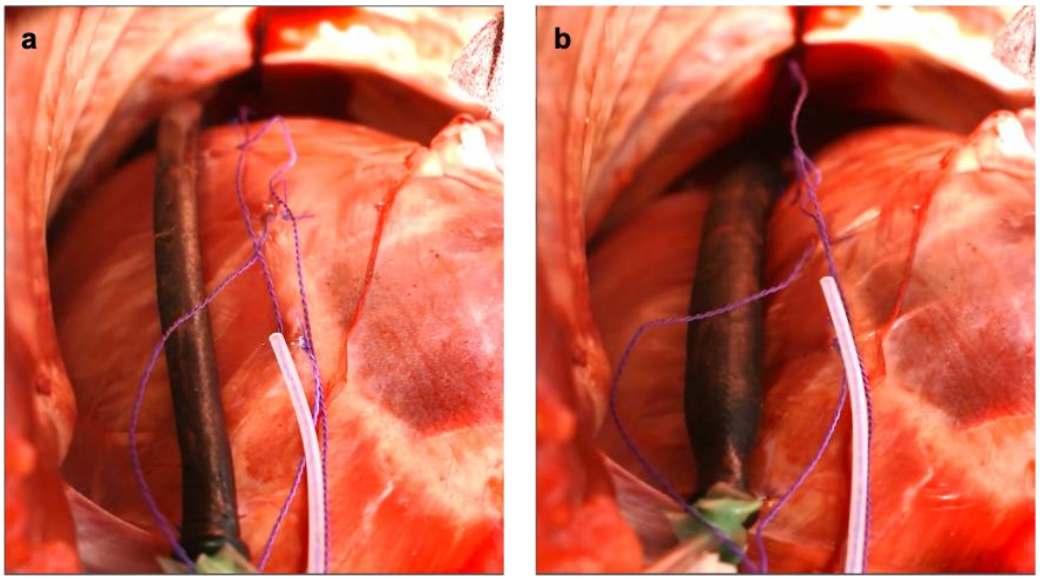

Fig. S1. Visualization of an actuator in situ. Supradiaphragmatic images of a single McKibben actuator placed *in situ* on the right hemidiaphragm in an (a) unpressurized and (b) pressurized (20 psi) state. The top of the images is the dorsal side. The bottom of the images is the ventral side. The anterior attachment point of the actuator is attached to the peristernal area. The posterior attachment point of the actuator is passed through the last intercostal space and sutured to the skin.

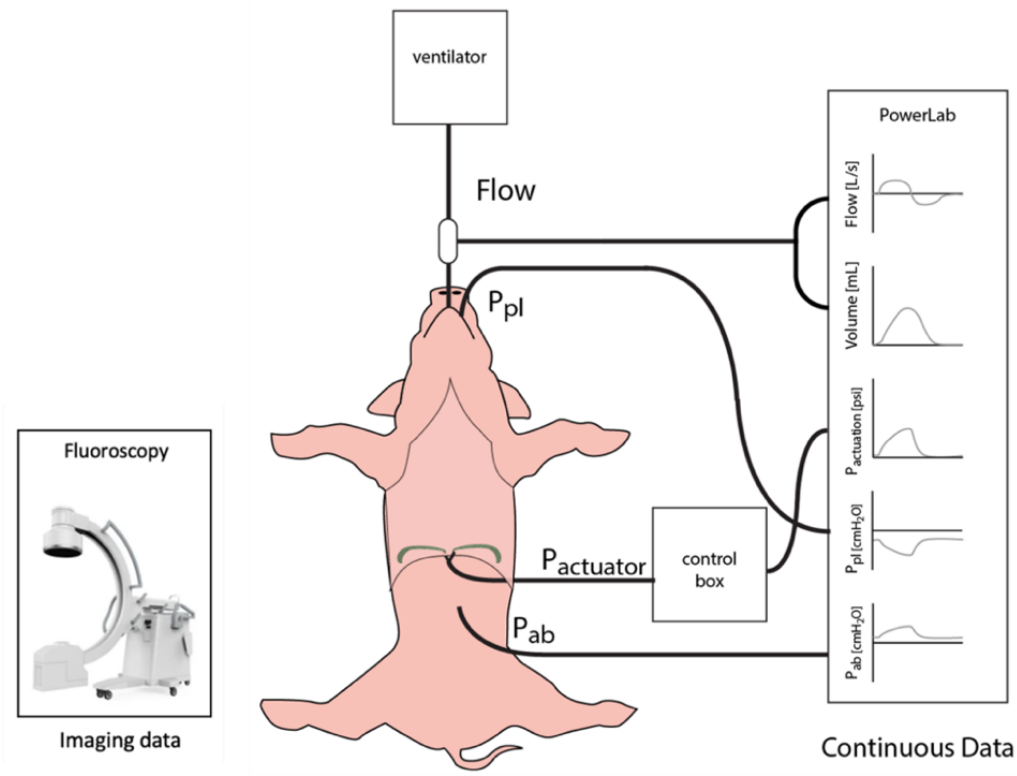

Fig. S2. Bioinstrumentation set up. Schematic of the bioinstrumentation setup to collect different types of physiological data. For the continuous data that was acquired via the PowerLab data acquisition system, idealized waveforms of one period of each signal are depicted.

Supplementary Notes

Controlling PAM actuator performance via pressurization

Actuator performance was characterized both *in vitro* and *in vivo* as described in the Methods in the main manuscript and the Supplemental Methods presented below.

Different input shapes explore the effect of rate of pressurization (Extended Data Fig. 1a-c). The fidelity to these idealized waveforms is limited by the control resolution of the electropneumatic regulators, and ultimately result in the output pressurization curves of Extended Data Fig. 1d-f. These actuation pressure curves ultimately govern the mechanical performance of the actuators. The actuators are characterized *in vitro* via tensile and flexural testing, as described in the Supplemental methods. The tensile force (Extended Data Fig. 1g-i) represents the contractile force applied to the points of attachment on the ribs, and the flexural force (Extended Data Fig. 1j-l) represents the force perpendicular to the actuator towards the diaphragm.

Different actuation pressure waveforms result in different displacements, (seen in the M-mode ultrasound in Extended Data Fig. 1m-o and quantified in Extended Data Fig. 1p), tidal volumes (Extended Data Fig. 1q) and different respiratory mechanics (Extended Data Fig. 1r). Notably, the square wave pressurization is distinct from the behavior of the curved wave and triangle wave, especially with regards to the average diaphragm displacement and the Campbell diagram. We note that the square wave achieves similar tidal volumes to the other waveforms while drawing more negative pleural pressures. The slope of the Campbell diagram, taken at the two points in the loop where $\frac{dV}{dP} = 0$, can be viewed as a representation of compliance of the system. A negative pleural pressure drives flow via the gradient from atmospheric pressure at the airway opening to the negative alveolar pressure, so we evaluate the absolute value of compliance. The slope generated by the square wave (12.1 mL/cmH_20) is considerably lower (i.e., the system is stiffer) than that of the curved (15.9 mL/cmH_20) and triangle wave (15.1 mL/cmH_20), which both have slopes that more closely resemble those that of spontaneous respiration (25.6 mL/cmH_20). These values are overall relatively stiff and are likely due to the low lung volumes for this subject. Qualitatively, we observe that the square wave results in “sharper” breaths that pull on the chest wall more aggressively compared to the gentler inflation of the curved and triangle wave, matching the much higher tensile forces generated by the square wave from *in vitro* testing.

The curved and triangular pressurization input are similar in their pressure-volume (PV) loops; however, the curved input achieves higher tidal volumes with marginally smaller levels of diaphragm displacement (Extended Data Fig. 1p-r), which could be attributed to the shorter time in which the actuator operates at a high pressure filled state which may not provide enough time for lung filling. Overall, the curved waveform used in the majority of the study (Fig.2-7 in the main text) represents a pressurization scheme that aims to combine the benefits of the square wave and triangular wave, generating the best tidal volumes and biomimetic PV loops.

PAM performance can also be tuned via depth of pressurization by scaling the input curved waveform shown in Extended Data Fig. 2a to different peak pressures (5, 10, 15, and 20 psi), the resulting actuator pressure waveforms are shown in Extended Data Fig. 2a-d. The relationship between pressurization and forces generated is linear (Extended Data Fig. 2e,f) which corroborates previous McKibben characterization work[24]. We characterize the response of one subject to the varying degrees of pressurization. The degree of pressurization has a positive, but nonlinear effect on the amount of diaphragm displacement generated (Extended Data Fig. 2g-k). In this subject, we demonstrate tunability of the degree of augmentation via changes in pressurization, with the greatest range of

responsiveness being between 0 and 10 psi. Additional increases taper off between 10 and 20 psi, which matches the understanding of how McKibben actuators operate, as they first expand and fill to their maximum volume, achieving maximum contraction, and beyond that they increase force generation[24]. In terms of respiratory mechanics, the degree of pressurization does not have a large effect on the change in pleural pressure (Extended Data Fig. 2m) unlike the different waveform shapes in Extended Data Fig. 2p.

Notably, interanimal variability is undeniably a factor contributing to overall performance, as evident in the varied responsiveness to the device seen in Fig. 3. Even in a case of low augmentation, we saw a nonlinear but tunable response to different levels of pressurization. The absolute degrees of augmentation shown in Extended Data Fig. 2k-m will obviously not hold across different animals, but we expect that the relative effect of tuning pressure should.

Complete arterial blood gas results

Extended Data Table 1 depicts ABGs taken during the respiratory challenges depicted in Fig. 5 with (a) independent actuation, (b) synchronized actuation, and (c) synchronized actuation after 2 minutes of unsupported ventilation. During (a), we observe a progressive blood acidification, a consequence of increasing P_aCO_2 (respiratory acidosis). In parallel, HCO_3 increases, and is an adaptative mechanism of the organism to correct pH value. However, this compensatory mechanism only partially helps controlling pH. During synchronized actuation (b), P_aCO_2 remains constant around the upper level of the normal range. We see a progressive acidification of the blood, whose main primary cause is a decrease in HCO_3 (metabolic acidosis). For respiratory challenge (c), ABGs shows a clear respiratory acidosis (elevated P_aCO_2) with partial compensatory mechanism (increase in HCO_3) during the unsupported ventilation phase. While actuating, P_aCO_2 decreases, as well as HCO_3, resulting in a controlled pH. At the end of the trial, P_aCO_2 slightly increases with a corresponding HCO_3 compensation. P_aO_2 and O_2 saturation (S_aO_2) remained in the normal range across all experiments.

Further data on the timing alignment analysis

As discussed in the main manuscript in the section entitled “Factors in optimizing synchronization”, there are many different alignment factors that can be analyzed (Fig. S3). One additional metric of interest is the relationship between the start of actuation (P_0) and the start of inspiration (V_0). Because the triggering system presented here relies on the beginning of inspiration for triggering, this is a metric that we hypothesized would be influential. We find no linear relationship between (P_0-V_0) and the tidal volume or the peak inspiratory flow (Fig. S4). Although we see a clustering effect in Fig. S4a,c, within the clusters, there are no linear relationships. The clusters themselves can be understood as two categories of actuation. Actuation that occurred early (likely falsely triggered) with a negative P_0-V_0 value and actuation that occurred in an appropriately synchronized fashion. With this distribution of behavior within one respiratory challenge, the data actually resembles the data from comparing

independent and synchronized trials (Fig. 5e,f). If we solely look at the data with a positive P_0-V_0 for all of Fig. 4, we find these clusters to both lack any linear relationship internally. This contrasts with the linear relationships found relating P_0 and V_{pk}.

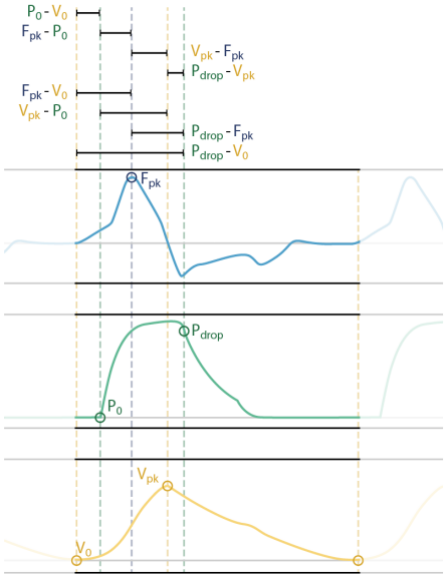

Fig. S3. Alignment metrics. Schematic depicting many of the alignment metrics derived from the flow, pressure, and volume waveforms that can be used for synchronization.

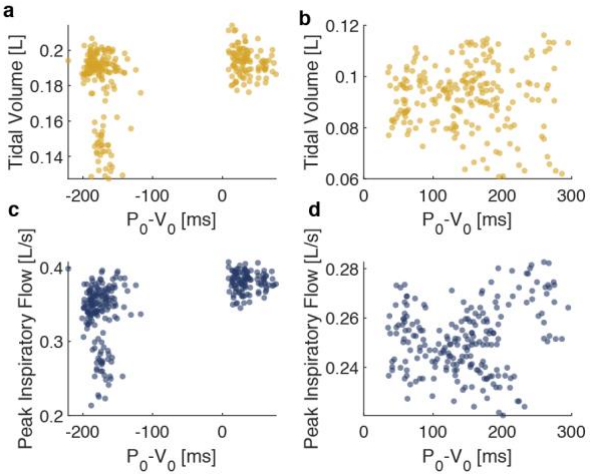

Fig. S4. Effect of the alignment of P_0-V_0 on flow and volume. a,b, A scatter plot of peak inspiratory volume as it relates to the time between P_0 and V_0 for one respiratory challenge with an (**c**) intact phrenic nerve and with a (**d**) severed phrenic nerve. **e,f,** A scatter plot of tidal volumes as it relates to the time between P_0 and V_0 for one respiratory challenge with an (**e**) intact phrenic nerve and with a (**f**) severed phrenic nerve. All data is taken from the same subject. Each dot represents data from one breath.

Considerations for PAM materials selection

Due to the acute nature of the study, we did not test the biocompatibility of the actuators. We used commercially available materials for ease of prototyping. In our design process, we did select materials with consideration of their future biocompatibility. PET, which makes up the mesh of our actuator, was chosen for its mechanical strength and chemical stability and has been used as a biocompatible material for vascular prostheses under the trade name Dacron[50,51]. Polyurethanes have been used in many biomedical applications for their biocompatibility and mechanical stability.[20,52,53] The thermoplastic elastomer of the balloon has been used in research studies creating patient specific valves[20] and neurosurgical tools[57]. Overall, the mechanical nature of our device is agnostic to specific material chemistry beyond the mechanical properties of different materials. Therefore, these components can easily be substituted for regulatory-approved biomaterials.

Supplementary Methods

McKibben Pneumatic Artificial Muscle (PAM) Manufacturing

The McKibben actuators used in this study consist of a thermoplastic elastomer bladder (Stretchlon 200, FibreGlast Developments Corp., Brookville, OH, USA), a thermoplastic polyurethane tubing (1/8" Tubing, 5648K226, McMaster-Carr, Inc, Elmhurst, IL, USA) and a poly(ethylene terephthalate) (PET) expandable braided mesh (PTO0.25BK, TechFlex, Inc., Sparta, NJ, USA). These actuators were sized to fit our 30-40 kg Yorkshire Swine.

First, the internal bladder was fabricated and coupled with the airline. The elastomeric bladder was formed by heat-sealing. Two layers of thermoplastic elastomer were aligned on top of a 3D-printed mold (Objet 20 Pro Stratysys, Ltd., Eden Prairie, MN, USA) and heat sealed with a heat press (Fancierstudio, Hayward, CA, USA) at 300°F for 5 s. The 3d printed mold yielded a bladder with dimensions 20 cm by 5 cm with a negative space for the airline measuring 1/8 in wide to accommodate the outer diameter of the tubing. After heat sealing, the polyurethane tubing was inserted into the airline opening. This junction was sealed with a urethane adhesive (Ure-Bond II, Smooth-On, Inc, Macungie, PA, USA).

Next, the bladder was coupled with the expandable braided mesh (PTO0.25BK, TechFlex, Inc.). Mesh was cut to a relaxed length of 26 cm. The bladder was placed inside the tubular mesh. To constrain the two ends of the active contractile region of the actuator, Kevlar thread (McMaster-Carr, Inc, Elmhurst, IL, USA) was used to sew the mesh closed at the two endpoints of the actuator. The active contractile length of the relaxed mesh was set to 18 cm, the distance between the two Kevlar points of closure. At the end of this process, the two most terminal ends of the mesh were heated and fused together to

prevent fraying of the non-active ends of the mesh, resulting in an actuator with a total relaxed length of 25cm.

After fabrication, actuators were subject to fatigue testing of >1000 cycles of pressurization to 20 psi as a quality control check to reveal manufacturing defects. During this testing, actuators were restrained on a custom 3-D printed scaffold—a modified flex fixture—mounted onto a stationary Instron testing setup (Fig. S5) that secured the actuator in an initially curved position.

Fig. S5. Modified flex fixture set up. Image of the actuator fixed to a custom 3d-printed modified flex fixture setup used for mechanical characterization and fatigue testing.

McKibben PAM Mechanical Characterization Methods

The forces generated by the McKibben actuators were characterized by two experimental methods. One method used standard fixed length contractile (isometric) measurements. Each end of the actuator was fixed to standard Instron tensile grips with the actuator at its relaxed length. The actuator was pressurized to 20 psi and its contractile force was measured.

Additionally, the McKibben actuators were placed into a custom modified flexural fixture, described in Fig. S5. Upon actuation, the contraction of the actuator pushed the actuator body into the 3-D printed convex component, providing a resistance to actuator straightening. This was intended to measure the bending load and simulate a resistive load of the dome of the diaphragm, although this set up represented a higher resistance than the dynamic and compliant diaphragm.

Prior to use, actuators underwent fatigue testing in this in the modified flex fixture set up shown in Fig. S5. Actuators that survived >1000 cycles of pressurization to 20 psi via the standard curved input waveform on the benchtop did not fail during the subsequent >1000 cycles of pressurization to 20 psi in the *in vivo* studies. The actuators that underwent the greatest total number of cycles withstood >3000 cycles and were still intact at the end of use.

PAM contraction and mechanical performance is determined by the controlled pressurization of the actuators. Preset pressurization waveforms are programmed into the microcontroller of the control system and given as an input to the electropneumatic regulators. We characterize the actuator behavior for different shapes and depths of pressurization.

Three different input shapes are shown in Extended Data Fig. 1a-c. All three waveforms represent a single breath with a timescale of 33 breaths per minute (1.82s per breath), an inspiratory time to expiratory time ratio (I:E) of 0.5, and a maximum pressurization of 20 psi. Extended Data Fig. 1a represents our curved waveform constructed to replicate native respiratory waveforms when used to drive respiration in our previously reported respiratory simulator[56]. Extended Data Fig. 1b represents the corresponding square wave to the above parameters. Extended Data Fig. 1c represents a triangle wave intended to mimic the rise and fall of the curved waveform.

To investigate the effect of depth of pressurization, the curved waveform of Extended Data Fig. 1a is scaled to different levels of pressurization (5, 10, 15, 20 psi).

Supplementary References

57. Amadeo, T. *et al.* Soft Robotic Deployable Origami Actuators for Neurosurgical Brain Retraction. *Front. Robot. AI* **8**, 437 (2022).